

Near-infrared spectroscopy of extreme BAL QSOs from the QUBRICS bright quasar survey

Guido Cupani,^{1,2*} Giorgio Calderone¹, Pierluigi Selvelli¹, Stefano Cristiani^{1,2,5}, Konstantina Boutsia³, Andrea Grazian⁴, Fabio Fontanot^{1,2}, Francesco Guarneri^{1,6}, Valentina D’Odorico^{1,2,7}, Emanuele Giallongo⁸, and Nicola Menci⁸

¹INAF–Osservatorio Astronomico di Trieste, Via Tiepolo 11, I-34143 Trieste, Italy

²IFPU–Institute for Fundamental Physics of the Universe, via Beirut 2, I-34151 Trieste, Italy

³Las Campanas Observatory, Carnegie Observatories, Colina El Pino, Casilla 601, La Serena, Chile

⁴INAF–Osservatorio Astronomico di Padova, Vicolo dell’Osservatorio 5, I-35122 Padova, Italy

⁵INFN–National Institute for Nuclear Physics, via Valerio 2, I-34127 Trieste, Italy

⁶Dipartimento di Fisica, Sezione di Astronomia, Università di Trieste, via Tiepolo 11, I-34131 Trieste, Italy

⁷Scuola Normale Superiore, piazza dei Cavalieri, I-56126 Pisa, Italy

⁸INAF–Osservatorio Astronomico di Roma, via Frascati 33, I-00078 Monte Porzio Catone, Italy

Accepted XXX. Received YYY; in original form ZZZ

ABSTRACT

We report on the spectral confirmation of 18 QSO candidates from the “QUasars as BRIght beacons for Cosmology in the Southern hemisphere” survey (QUBRICS), previously observed in the optical band, for which we acquired new spectroscopic data in the near-infrared band with the Folded-port InfraRed Echellette spectrograph (FIRE) at the Magellan Baade telescope. In most cases, further observations were prompted by the peculiar nature of the targets, whose optical spectra displayed unexpected absorption features. All candidates have been confirmed as bona fide QSOs, with average emission redshift $z \approx 2.1$. The analysis of the emission and absorption features in the spectra, performed with ASTROCOOK and QSFIT, reveals that the large majority of these objects are broad-absorption line (BAL) QSOs, with almost half of them displaying strong Fe II absorption (typical of the so-called FeLoBAL QSOs). The detection of such a large fraction of rare objects (which are estimated to account for less than one percent of the general QSO population) is interpreted as an unexpected (yet favourable) consequence of the particular candidate selection procedure adopted within the QUBRICS survey. The measured properties of FeLoBAL QSOs observed so far provide no evidence that they are a manifestation of a particular stage in AGN evolution. In this paper we present an explorative analysis of the individual QSOs, to serve as a basis for a further, more detailed investigation.

Key words: quasars: general — emission lines — absorption lines, galaxies: nuclei

1 INTRODUCTION

The study of luminous quasars (QSOs) at medium to high redshift is pivotal for a wide range of science cases in astrophysics, observational cosmology, and even fundamental physics. QSOs are among the best faraway beacons in the Universe, literally shedding light in the otherwise virtually invisible inter-galactic medium along their line of sight, but are also interesting in themselves, as the most apparent manifestation of the super-massive black hole growth in the early stage of galaxy evolution. The analysis of absorption and emission features in the optical and near-infrared (NIR) spectra of QSOs plays a key role in understanding the physical conditions of the primordial universe, the interplay between galaxies and large-scale structure, the mechanism of reionization, and related issues; it also helps constraining the primordial abundance of elements, the power spectrum

of dark matter, the possible variation of fundamental constants across time, and the validity of General Relativity. All these undertakings rely on the availability of bright QSOs at $z \gtrsim 2.5$ across the whole sky.

The QUBRICS survey (“QUasars as BRIght beacons for Cosmology in the Southern hemisphere”) was started in 2018 to even up a significant lack of identified QSOs in the Southern Hemisphere. The project entails the selection of QSO candidates from public databases, using innovative machine-learning techniques (Calderone et al. 2019; Guarneri et al. 2021) and their spectral confirmation through direct observation in the optical band (Calderone et al. 2019; Boutsia et al. 2020). The result is a growing catalogue of some 400 newly discovered bright QSOs, which will significantly enhance the feasibility of a redshift drift measurement with future facilities (the so called Sandage Test; Boutsia et al. 2020) and were already used to put stronger constraints on the bright end of the QSO luminosity function (Boutsia et al. 2021).

* E-mail: guido.cupani@inaf.it

Quite understandably, optical spectroscopy alone was not always sufficient to confirm or reject candidates as bona-fide QSOs. In particular, a number of candidates revealed notable absorption features that could not be explained as arising from structures either associated with the emitting AGN or located along the line of sight, given the scarce information provided by the emission component. We refer to these candidates as the “QUBRICS Irregular and Peculiar” (QUIP) targets. In other cases, a relative featureless optical spectra prevented a secure determination of the emission redshift (these unidentified objects are dubbed non-QUIP). To properly assess all these objects (QUIP and non-QUIP), we started a NIR observational campaign using the Folded-port InfraRed Echellette spectrograph (FIRE) at the Magellan Baade telescope. All the 18 targets observed so far in the NIR have been securely confirmed as QSOs through the observation of their Balmer series and/or other emission lines, with luminosities at 5100 \AA ranging from about $1.5 \times 10^{46} \text{ erg s}^{-1}$ to $4.4 \times 10^{47} \text{ erg s}^{-1}$.

A relevant outcome of this observational campaign is that a large fraction of QUIPs appear to be broad-absorption line QSOs (BALQs), and in particular show strong intrinsic absorption from either high-ionization species like C IV and Si IV (HiBALQs), or low-ionization species like Mg II and Al III (LoBALQs), and occasionally Fe II (FeLoBALQs). BALQs form an inherently interesting, yet not fully understood class of objects. Their characteristically strong absorption features, conventionally wider than 2000 km s^{-1} and at least 10 percent below the continuum level (Weymann et al. 1991), are often blueshifted to velocities up to tens of thousands kilometers per second with respect to the QSO emission redshift, and are recognized as a signature of energetic AGN outflows (e.g. Foltz et al. 1983; Weymann et al. 1991), which are assumed to play an important role in quenching star formation in the host galaxies and self-regulating the growth of super-massive black holes (e.g. Silk & Rees 1998; Di Matteo et al. 2005; Fabian 2012; Kormendy & Ho 2013). A proper understanding of such feedback mechanism is fundamental to explain the observed properties of QSO host galaxies and to constrain the AGN-galaxy co-evolution. It is still unclear whether the strong outflows observed in BALQs represent a specific stage in the AGN evolution, or an ubiquitous feature that becomes apparent only when the QSO is observed at the right orientation (see e.g. Schulze et al. 2017, and references therein). This is particularly true for the LoBALQ and FeLoBALQ subclasses, as different pieces of evidence from these objects support either the evolution scenario or the orientation scenario. LoBALQs appear to be more reddened than other QSOs (e.g. Sprayberry & Foltz 1992; Reichard et al. 2003; Farrah et al. 2007), and this is consistent with the idea that they are young merger-induced QSOs caught in the process of blowing off their dust envelope, quenching star formation as a result (Farrah et al. 2012; Faucher-Giguère et al. 2012). However, the star formation rate in LoBALQ host galaxies does not appear significantly different (Lazarova et al. 2012; Violino et al. 2016) and there is no consensus about LoBALQs actually exhibiting larger Eddington ratios, as their younger age would imply (compare e.g. Schulze et al. 2017; Urrutia et al. 2012).

The identification of 7 previously unknown FeLoBALQs among the QUIPs represents a noteworthy addition to a class of objects estimated to account for only a tiny fraction of the whole QSO population (Trump et al. 2006; Dai et al. 2012). We present in this paper a preliminary analysis of all the NIR spectra acquired so far within the QUBRICS survey, with a specific focus on explaining the reasons for the relatively high (Fe)LoBALQ detection rate (which has been recently observed also in the SkyMapper survey, Wolf et al. 2019). Despite the limitations set by the data sample, we are able to

provide values of black hole mass and Eddington ratio for most of the targets, which give no indication that the FeLoBAL subsample is accreting at a higher ratio than other QSOs (as an evolutionary scenario would suggest). The analysis, performed with the packages ASTROCOOK (Cupani et al. 2020b) and QSFIT (Calderone et al. 2017) is aimed at providing the basis for a further, more detailed analysis of the individual targets.

The paper is organized as follows: in section 2 we describe how data were acquired and treated; in section 3 we present a qualitative assessment of the spectra; in section 4 we discuss the statistics of the sample, with reference to the QUBRICS catalogue as a whole and to the general QSO population; finally, in section 5 we draw the conclusions of the campaign. Magnitudes are expressed in the AB systems. Atomic transitions are denoted by their ionization state (I for neutral species, II for singly ionized species, etc.) and, when required to avoid ambiguity, by their rest-frame vacuum wavelength in \AA preceded by λ (e.g. H α $\lambda 6563$).

2 DATA TREATMENT

2.1 Acquisition

In Calderone et al. (2019, hereafter Paper I) we presented the first results of our survey, aimed at identifying previously unknown QSOs with $i \leq 18$ at $z \geq 2$ in the Southern Hemisphere using the photometric information from existing databases (SkyMapper, Gaia DR2, WISE, and 2MASS). We implemented a new method based on the Canonical Correlation Analysis and extracted a preliminary list of about 1500 QSO candidates, 54 of which were spectroscopically confirmed as QSOs at $z > 2.5$. The survey was further extended as documented in Boutsia et al. (2020, hereafter Paper II), bringing the number of confirmed QSOs at $z > 2.5$ to 224 and the total number of confirmed QSOs to 390.

Alongside these sources, which were securely confirmed by spectroscopic observations in the optical band (“flag A”), the survey produced a remaining 79 candidates (“flag B”) whose exact nature was still uncertain, for a variety of reasons: i) spectra were noisy and could not provide a clear redshift indication; ii) spectra showed broad and numerous absorption features that could not be unambiguously associated to a single redshift solution; 3) only a single emission line was visible, preventing a secure identification.

The observational campaign discussed in this paper was aimed at assessing the nature of 16 of the brightest flag-B candidates, including 13 targets with peculiar absorption features (QUIPs) and 3 other bright targets. The details of the observations, including both optical and NIR observations, are given in Table 1. Two flag-A candidates exhibiting QUIP features were added to the sample, bringing the total to 18. We acquired a total of 26 optical spectra (taking into account targets that were observed more than once) and 18 NIR spectra.

The acquisition of the optical spectra is described in Paper I and Paper II; here we summarize it as follows:

(i) 7 targets were observed with EFOSC2 at ESO-NTT during ESO period P103 (April–September 2019, PI A. Grazian, proposal 0103.A-0746). Grism #13 was used, with a wavelength range $\lambda \approx 3700 \text{ \AA} - 9300 \text{ \AA}$ and a central-wavelength FWHM of $\sim 21 \text{ \AA}$ or $\sim 1000 \text{ km/s}$ ($R \approx 300$), with a $1.5''$ slit. The range of exposure times was 360 s–600 s.

(ii) 7 targets were observed with LDSS3 at the Magellan Clay Telescope between September and November 2019. Grism VPH-ALL was used, with a wavelength range $\lambda \approx 4250 \text{ \AA} - 10\,000 \text{ \AA}$ and a

resolution of ~ 860 (FWHM $\approx 8 \text{ \AA}$ or $\sim 350 \text{ km/s}$), with a $1.0''$ slit. The range of exposure times was 400 s–600 s.

(iii) 6 targets were observed with WFCCD at the du Pont Telescope between August and September 2019. The blue grism was used, with a wavelength range $\lambda \approx 3600 \text{ \AA}$ – 7600 \AA and a dispersion of 2 \AA/pixel , together with a $1.6''$ slit, achieving a resolution of ~ 800 (FWHM $\approx 6 \text{ \AA}$ or $\sim 375 \text{ km/s}$). The range of exposure times was 400 s–900 s.

(iv) 5 targets were observed with MagE at the Magellan Baade Telescope between October 2018 and November 2019, with a wavelength range $\lambda \approx 3300 \text{ \AA}$ – $10\,000 \text{ \AA}$ and a slit of $0.85''$ or $1.0''$, achieving a resolution from 4100–4800 (FWHM $\approx 1.4 \text{ \AA}$ – 1.6 \AA or 60 km/s – 70 km/s). The range of exposure times was 1200 s–1800 s.

(v) 1 target was observed with DOLORES (LRS) at the Telescopio Nazionale Galileo in June 2021, with a wavelength range $\lambda \approx 3500 \text{ \AA}$ – 8000 \AA and a slit of $1.5''$, achieving a resolution of ~ 390 (FWHM $\approx 15 \text{ \AA}$ or $\sim 770 \text{ km/s}$). The total exposure time was 580 s.

The acquisition of NIR spectra was carried out with the FIRE spectrograph at the Magellan Baade Telescope between December 2018 and November 2019. The high throughput prism mode was used, with slits of $0.6''$ or $1.0''$; nominal resolution ranged from $R \approx 400$ – 500 in the J band to $R \approx 200$ – 300 in the K band. Four to six exposures of $t_{\text{exp}} \approx 126 \text{ s}$ were taken for each target, depending on the observing conditions, for a total exposure time ranging from 510 s to 760 s.

2.2 Reduction and analysis

The reduction of optical spectra taken with WFCCD, EFOSC2, and LDSS-3 has been described in Paper I and Paper II. MagE spectra were reduced using the CarPy pipeline¹ (Kelson 2003; Kelson et al. 2000). The CarPy product is a sky subtracted, wavelength calibrated spectrum for each separate order. Every night a target was observed, an associated spectro-photometric standard star was also observed and used for relative flux calibration. Flux calibration was performed with IRAF (Tody 1993) routines. The task *standard* was used to calibrate the flux of a standard star based on tabulated calibration data included in the IRAF database, consisting of wavelengths, calibration magnitudes and bandpass widths. The output was then used by the task *sensfunc* in order to obtain the system sensitivity as a function of wavelength. This task also produces a revised extinction function based on the residuals to the input extinction table. In this case the *CR10* extinction table has been used. Finally, the task *calibrate* applies the sensitivity function to the source spectra that are now corrected for extinction and calibrated to the correct flux scale. The flux calibrated spectrum of each order has then been combined using the IRAF task *scombine*, to obtain the 1D spectrum over the full wavelength range.

NIR spectra taken with the FIRE spectrograph were reduced with the FireHose IDL pipeline (Gagné et al. 2015), and in particular with the procedure designed for prism spectra, which includes flat-fielding, manual wavelength calibration, and optimal extraction. A set of reference stars were also reduced with the same procedure, to be used for telluric absorption removal and flux calibration. Each star was individually associated with a given QSO and observed immediately before or after the QSO itself.

The set of reduced spectra were post-processed with the ASTROCOOK package² for QSO spectral analysis (Cupani et al. 2018, 2020a; Cupani et al. 2020b). The post-processing included five steps:

(i) *Coaddition of the NIR spectra.* The extracted NIR exposures were combined into a single spectrum and rescaled to matching count values. ASTROCOOK creates a combined spectrum by retaining all the information from the contributing exposures, including the wavelengths and sizes of individual pixels. This combined spectrum was then rebinned into a log-wavelength grid with step $\Delta v = c \Delta \log \lambda = 50 \text{ km s}^{-1}$; $\Delta \lambda \approx 1.67 \text{ \AA} \times (\lambda / 10\,000 \text{ \AA})$, optimizing the wavelength range to the instrument setup adopted for each night. The reference star spectra were rebinned to the same wavelength grid of the associated QSO spectra, to maintain the compatibility.

(ii) *Telluric absorption removal and flux calibration of the NIR spectra.* Reference star spectra were normalized to a black-body spectrum with proper effective temperature. The spectra were “cleaned” by visually identifying their most prominent absorption features and clipping them out. The resulting spectra are ideally free from features intrinsic to the stars and contain only the signatures of the telluric absorption and the instrument response. QSO spectra were divided by these calibrators, respecting the association between each QSO and the star observed closest in time. It is worth remarking that the flux calibration performed in this way is only relative: the spectral shape of the QSO is reconstructed, but it is not rescaled to proper physical units and it differs from the actual flux density profile by a constant factor.

(iii) *Coaddition of the optical spectra.* Optical spectra were flux calibrated (at least in a relative sense) during reduction, and in general they are much less affected by telluric absorption than NIR spectra. Reduced exposures from different instruments were thus directly combined into a flux calibrated spectrum, rescaling their flux to matching values in the superposition regions. Noisy regions at the ends of the spectra were cut out before coaddition. The combined spectrum was then rebinned into a log-wavelength grid with step $\Delta v = 300 \text{ km s}^{-1}$; $\Delta \lambda \approx 10 \text{ \AA} \times (\lambda / 10\,000 \text{ \AA})$, to accommodate for the different resolving power of the instrument and avoid oversampling.

(iv) *Merging of the optical and NIR spectra.* The combination and rescaling procedure was adopted also to merge optical and NIR spectra of each target into a final spectrum. In some cases, the combination procedure highlighted a discrepancy between the wavelength calibration in the two bands. As the discrepancy was within the estimated accuracy of manual wavelength calibration as implemented by the FireHose pipeline, we decide to correct it by rigidly shifting the NIR spectrum along wavelengths to match the optical spectrum, using shared features as a reference. The typical shift was of $\sim 10 \text{ \AA}$, never exceeding 40 \AA . The combined spectrum was further down-sampled into a log-wavelength grid; the step was $\Delta v = 500 \text{ km s}^{-1} \approx 16.7 \text{ \AA} \times (\lambda / 10\,000 \text{ \AA})$ for all targets, except for J1318–0245, which was resampled at $\Delta v = 800 \text{ km s}^{-1} \approx 26.7 \text{ \AA} \times (\lambda / 10\,000 \text{ \AA})$ in account of the lower resolution of the LRS optical spectrum.

(v) *Photometric adjustment of flux calibration.* Merged spectra were further calibrated using photometry from the SkyMapper Data Release 1 (Wolf et al. 2018). Flux densities were integrated within the SkyMapper photometric bands and compared with the available magnitudes. We assumed that the relative flux calibration performed in the previous steps was good enough to reconstruct the shape of the spectrum up to a normalization factor, and we computed it as the average of the correction factors extracted from the available bands. The resulting spectra are flux-calibrated in an absolute sense and

¹ <https://code.obs.carnegiescience.edu/mage-pipeline>

² <https://github.com/DAS-OATs/astrocook>

Table 1. Summary of the observations of QUIP targets, with approximate exposure times, sorted by ascending RA. SkyMapper ID from Data Release 1 (Wolf et al. 2018) are provided for reference.

Name	QUBRICS ID	SkyMapper ID (DR1)	Flag	RA	Dec	mag _i	EFOSS2 t_{exp}	LDSS3 t_{exp}	WFCCD t_{exp}	MagE t_{exp}	LRS t_{exp}	FIRE t_{exp}	slit
J0008–5058	963183	317765879	B	00:08:11.96	–50:58:44.95	17.591	420 s			1800 s		760 s	1.0''
J0010–3201	1030576	6425629	B	00:10:40.66	–32:01:11.14	16.770		600 s	600 s			510 s	1.0''
J0140–2531	1035925	6814119	B	01:40:30.83	–25:31:37.48	17.291	360 s					510 s	1.0''
J0407–6245	921925	314058510	B	04:07:36.82	–62:45:49.28	16.346		400 s				510 s	1.0''
J0514–3854	999243	11288048	B	05:14:21.33	–38:54:42.57	16.888		600 s	500 s			510 s	1.0''
J1215–2129	814912	64056228	B	12:15:02.40	–21:29:14.13	16.741	600 s					760 s	0.6''
J1318–0245	823202	65974091	B	13:18:33.31	–02:45:36.22	17.876					580 s	1010 s	0.6''
J1503–0451	882537	100099370	B	15:03:50.13	–04:51:45.09	16.896	600 s					510 s	0.6''
J2012–1802	1052318	170868221	B	20:12:25.59	–18:02:46.77	17.092	360 s					760 s	1.0''
J2018–4546	1089108	306376125	A	20:18:47.29	–45:46:48.42	16.462		600 s		1800 s		760 s	0.6''
J2105–4104	891578	307248146	B	21:05:26.94	–41:04:52.58	17.099	600 s		600 s			760 s	1.0''
J2134–7243	990244	305553291	B	21:34:58.78	–72:43:11.83	16.889		600 s		1800 s		760 s	0.6''
J2154–0514	862715	4025749	B	21:54:56.69	–05:14:50.37	17.778		600 s				760 s	1.0''
J2157–3602	875768	397340	A	21:57:28.21	–36:02:15.11	17.367			900 s			760 s	0.6''
J2222–4146	917913	1098401	B	22:22:26.09	–41:46:29.99	16.228		600 s		1200 s		760 s	0.6''
J2255–5404	892403	308459017	B	22:55:08.37	–54:04:14.01	16.975			400 s			760 s	1.0''
J2319–7322	846931	305771865	B	23:19:31.05	–73:22:56.45	17.263			400 s			510 s	1.0''
J2355–5253	962517	308944978	B	23:55:52.05	–52:53:50.37	17.665	420 s			1800 s		760 s	0.6''

are suitable to infer the properties of the emitting sources from flux measurements.

(vi) *Redshift estimation.* A first estimate of the emission redshifts was obtained by shifting an emission line mask along the spectra and visually finding the better alignment with the QSO emission features. The mask contained transitions from the Lyman (Ly α λ 1216, Ly β λ 1026, Ly γ λ 973) and Balmer series (H α λ 6563, H β λ 4861, H γ λ 4340) and metal transitions (N v λ 1241; Si ii λ 1304; Si iv λ 1398; C iv λ 1549; Al iii λ 1859; Mg ii λ 2800); the list of transitions was adjusted to match the actual presence of features and the wavelength coverage of the spectrum. The redshift estimation was then improved by shifting each merged spectrum to rest frame and computing the cross-correlation with the above-mentioned QSO spectrum template in the region of the Balmer series emissions. The uncertainty of the estimation was assessed with a bootstrap method similar to the one described by Peterson et al. (1998): we created an ensemble of 100 realizations for each merged spectrum using random sampling with replacement and determined the redshift and its error from the statistics of the cross-correlation maxima over the ensemble. All the errors were below 10^{-3} ; combined with the uncertainty on wavelength calibration, we conservatively assume a maximum redshift uncertainty of ± 0.01 for all our targets.

(vii) *Reddening correction.* Flux calibrated spectra were cleaned from spikes and other spurious features and corrected for both Galactic and intrinsic extinction, using the parametrization by O’Donnell (1994) and assumed a total selective extinction $A(V)/E(B-V) = 3.1$. Intrinsic extinction was estimated by shifting each merged spectrum to rest frame and comparing it with a QSO spectrum template (combined from Vanden Berk et al. 2001 and Glikman et al. 2006). We tested values of intrinsic colour excess $E(B-V)$ between 0.00 and 0.30, with a step of 0.05³, and visually selected the value that yielded the best agreement with the template in the full spectral range. The $E(B-V)$ values used to de-redden the spectra (both Galactic and intrinsic) are listed in Table 2. We also created composite spectra

³ Given the quality of the data, we refrained from determining the intrinsic $E(B-V)$ at a better precision, considering that its impact on the continuum normalization at wavelength larger than ~ 4500 Å rest-frame would have been nevertheless negligible; see subsection 2.3.

for the two groups of targets described in section 3. These composite spectra were obtained from rest-frame spectra (de-reddened and non de-reddened) by rebinning them to a fixed log-wavelength grid with step $\Delta\nu = c\Delta \log \lambda = 800 \text{ km s}^{-1}$; $\Delta\lambda \simeq 16.7 \text{ \AA} \times (\lambda/10\,000 \text{ \AA})$, normalizing the flux at 3800 Å rest-frame, and computing their geometric mean.

Some of the target characteristics determined by this analysis are listed in Table 2. The whole analysis procedure was firstly run using the ASTROCOOK graphical user interface, to define the steps and the parameters. Once the procedure was frozen, it was translated into a set of JSON files and Bash scripts to allow for a cascade execution. Both the input data and the processing files are released together with the processed data as ancillary material to this paper (see “Data availability” below).

2.3 Modeling the broad band QSO emission

An estimate of the broad band continuum emitted by the QSO would require simultaneous observations spanning several bands at optical and NIR wavelengths. Here we attempt to estimate the slope and luminosity of the QSO continuum using just the NIR spectrum and the approach described in Calderone et al. (2017). In particular, we used the QSFIT⁴ package to constrain a global model spanning the whole wavelength range covered by the NIR spectrum, and simultaneously fitting all relevant spectral components. We excluded from the modeling the regions most affected by telluric absorption (13 500–14 500, 18 000–19 500, and $>25\,000$ Å in the observed frame) and most contaminated by metal absorption (<2800 Å rest-frame). The main model components are: the QSO continuum itself (modelled as a simple power law); the blended Fe ii and Fe iii emission lines at optical/ultraviolet (rest-frame) wavelengths; and the most prominent emission lines (Si iv, C iv, C iii λ 1909, Mg ii, H γ , H β , [O iii] λ 4959, 5007 and H α).

The best fit parameters and their 1- σ uncertainties (as obtained with the Fisher matrix method, i.e. by considering the square root of the diagonal elements of the covariance matrix) are shown in Table 2.

⁴ <https://qsfit.inaf.it/>

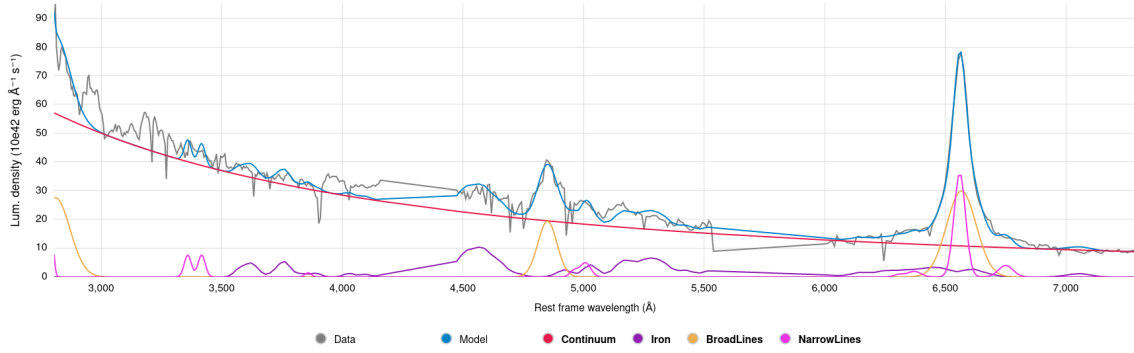


Figure 1. NIR spectrum of J2105–4104 and best fit model. Although the model does not account for all the features in the observed spectra, it still provides a reliable estimate of the broad band QSO continuum (here modelled as a power law). The two emission lines at 4861 Å and 6563 Å rest-frame are $H\beta$ and $H\alpha$, respectively.

An example of fitted model is shown in Figure 1. The spectral range used to fit the model was different for each QSO, depending on redshift and presence of telluric absorption.

The continuum slope was successfully estimated in 17 cases out of 18: the continuum of J0140–2531 was not compatible with a power-law profile since it shows systematically negative residuals at wavelengths larger than ~ 3300 Å (rest-frame), hence we decided to neglect the analysis for this target, rather than using a more complicated model, and maintain the uniformity of the procedure. The continuum of J2319–7322 is also uncertain, because it was constrained only for $\lambda > 4000$ Å; below this limit the shape was not compatible with a power-law profile, much like for J0140–2531 above.

The FWHMs and luminosities of the Balmer series lines were successfully estimated for at least one line in 16 cases out of 17, along with the corresponding luminosity at $\lambda = 5100$ Å. In the case of J2157–3602, the relatively high redshift prevented the observation of the Balmer series in the wavelength range covered by FIRE. In other cases, we could not obtain a reliable estimate of the parameters for all the emission lines since the profiles are affected by strong telluric absorptions, especially at wavelengths slightly shorter than the Mg II and $H\beta$ lines. The end-of-scale FWHM value of $15 \times 10^3 \text{ km s}^{-1}$ denotes the cases where the fitting procedure was not able to converge to a value below this figure. We regard these values as mere upper limits for the real FWHMs of the lines. Additionally, the $1-\sigma$ error of FWHM values does not take into account the uncertainty associated with the power-law continuum fitting and with other non-modeled emission features. Values of $L_{H\alpha}$, $L_{H\beta}$, and λL_{5100} are in principle affected by errors in the intrinsic $E(B - V)$ used in de-reddening; even an error as large as 0.05 would nevertheless produce only a $>2\%$ variation in the flux level at $\lambda \gtrsim 4500$ Å rest-frame, rendering it negligible when compared to the uncertainties resulting from fitting.

On the other hand, the Balmer decrement (ratio of integrated luminosities of $H\alpha$ and $H\beta$) is 2.9 ± 0.9 in agreement with, e.g., Lu et al. 2019. The distribution of continuum slopes is -1.89 ± 0.18 ($L_\lambda \propto \lambda^\alpha$) and the values show no dependence on redshift (see Figure 2).

3 OVERVIEW OF THE SPECTRA

Table 2 lists the main characteristics of the QUIPs, resulting from the analysis with ASTROCOOK and QSFit. In 13 out of 15 cases the redshift is firmly established by the detection of a strong $H\alpha$ emission line, frequently complemented by a comparably clear detection of $H\beta$ (11 cases out of 13) and $H\gamma$ (8 cases out of 13). Occasionally, the $H\beta$

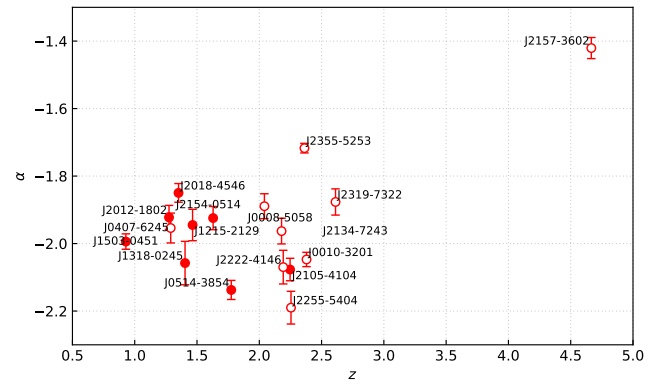


Figure 2. Broad band QSO continuum slope ($F_\lambda \propto \lambda^\alpha$) vs. source redshift for all the targets in our sample. FeLoBALQs (see subsection 3.1) are denoted with filled circles, while other targets are denoted with empty circles. Error bars are the $1-\sigma$ uncertainties, as derived from the Fisher matrix.

and $H\gamma$ lines fall within the strong telluric H_2O absorption band at ~ 14000 Å, but they are marginally detectable anyway.

The line mask described subsection 2.2 helped in visually identifying notable absorption systems. According to the classification given in Table 2, 14 out of 15 (93.3%) QUIPs are BALQs, either HiBALQs (5 out of 14, 35.7%) or LoBALQs (9 out of 14, 64.3%). 8 out of 9 LoBALQs (88.9%) show evidence of strong Fe II absorption (FeLoBALQs).

The spectra of the individual targets are shown at the end of the paper in Figure 6 (FeLoBALQs) and Figure 7 (non-FeLoBALQs). A description of the same targets in the two groups is given in subsection 3.1 and subsection 3.2, with targets sorted by their right ascension. Composite spectra for the two groups are displayed in Figure 3 (blue and green for FeLoBALQs and non-FeLoBALQs, respectively), superimposed to the individual spectra in transparency. Identified emission and absorption features are highlighted in the plots with dotted bars and described in the text moving bluewards of the QSO emission redshift to the observer.

In the formulae, we will refer to FeLoBALQs and non-FeLoBALQs with subscripts F and nF, respectively. We will also use H and L to refer to HiBALQs and LoBALQs specifically. Values of quantities labeled with these subscripts are the average and the standard deviation across the respective groups.

Table 2. Main characteristics of the observed targets after analysis. Q, H, L, and F are abbreviations for QUIP, HiBALQ, LoBALQ, and FeLoBALQ, respectively. No assigned class means that the target is neither a QUIP nor a (Hi/Lo/FeLo)BALQs. The determination of the emission redshift z_{em} is described in [subsection 2.2](#). The fit of the power-law index α to the continuum emission is discussed in [subsection 2.3](#).

QUBRICS ID	class	z_{em}	$E(B - V)$		α	FWHM $_{H\alpha}$ 10 ³ km s ⁻¹	FWHM $_{H\beta}$ 10 ³ km s ⁻¹	$L_{H\alpha}$ 10 ⁴² erg s ⁻¹	$L_{H\beta}$ 10 ⁴² erg s ⁻¹	λL_{5100} 10 ⁴⁴ erg s ⁻¹
			gal.	intr.						
J0008–5058	Q,H	2.041	0.014	0.10	-1.89 ± 0.04	7.5 ± 1.2	6.8 ± 1.1	2300 ± 200	$770 \pm 100.$	490 ± 20
J0010–3201	Q,H	2.379	0.013	0.00	-2.05 ± 0.02	8.4 ± 0.9	<15	2700 ± 200	$1300 \pm 150.$	500 ± 20
J0140–2531	Q	2.947	0.012	0.00						
J0407–6245	Q,L	1.289	0.032	0.00	-1.95 ± 0.04	6.3 ± 1.0	5.6 ± 1.1	500 ± 80	171 ± 27	200 ± 10
J0514–3854	Q,F	1.775	0.035	0.00	-2.14 ± 0.03	7.6 ± 0.8	14.7 ± 3.1	1130 ± 80	440 ± 130	330 ± 10
J1215–2129	Q,F	1.464	0.051	0.20	-1.94 ± 0.05	9.7 ± 1.3	13.8 ± 4.0	1620 ± 180	510 ± 150	610 ± 20
J1318–0245	Q,F	1.404	0.023	0.15	-2.06 ± 0.06	7.0 ± 2.2	4.7 ± 1.0	260 ± 70	180 ± 20	150 ± 6
J1503–0451	Q,F	0.929	0.081	0.15	-1.99 ± 0.02	7.6 ± 0.5	11.0 ± 0.9	920 ± 40	350 ± 30	182 ± 4
J2012–1802	Q,F	1.275	0.104	0.25	-1.92 ± 0.03	6.8 ± 0.7	6.9 ± 0.9	1550 ± 110	610 ± 70	470 ± 10
J2018–4546	Q,F	1.352	0.027	0.15	-1.85 ± 0.03	6.9 ± 0.8	10.2 ± 1.4	1320 ± 90	580 ± 70	510 ± 10
J2105–4104	Q,F	2.247	0.029	0.10	-2.08 ± 0.03	6.5 ± 0.5	5.0 ± 0.5	5000 ± 300	1780 ± 140	940 ± 30
J2134–7243		2.178	0.037	0.00	-1.96 ± 0.04	5.9 ± 1.1	10.3 ± 2.3	880 ± 140	620 ± 110	400 ± 20
J2154–0514	Q,F	1.629	0.022	0.20	-1.92 ± 0.03	7.4 ± 1.4	5.4 ± 0.8	860 ± 80	360 ± 60	330 ± 10
J2157–3602	Q,H	4.665	0.013	0.05	-1.42 ± 0.03					4400 ± 200
J2222–4146		2.192	0.013	0.00	-2.07 ± 0.05	9.3 ± 3.0	<15	1440 ± 290	1020 ± 210	650 ± 30
J2255–5404	Q,H	2.255	0.013	0.15	-2.19 ± 0.05	6.7 ± 0.7	8.5 ± 1.3	3700 ± 300	1860 ± 220	810 ± 40
J2319–7322	Q,H	2.612	0.025	0.00	-1.88 ± 0.04	6.5 ± 1.1	<15	1390 ± 190	1260 ± 140	620 ± 20
J2355–5253		2.363	0.013	0.00	-1.72 ± 0.01	2.6 ± 0.6	1.6 ± 1.9	550 ± 60	132 ± 42	310 ± 10

3.1 FeLoBAL QSOs

A significant fraction of QUIP targets (88.9%) shows BAL features from ions like Mg II, Al III, and Fe II, sometimes alongside absorption from higher-ionization ions like C IV, Si IV, and N V. Low-ionization BALQs with Fe II absorption systems, or FeLoBALQs, are a widely-investigated class of objects (see e.g. [Korista et al. 1993](#); [Farrah et al. 2007](#); [Faucher-Giguère et al. 2012](#)). Low-ionization BAL features have large column densities, thick enough to extend beyond the hydrogen ionization front ([Hazard et al. 1987](#)). FeLoBALQs in particular reach the highest column densities among BALQs ([Lucy et al. 2014](#)), in some cases resulting in a saturated trough bluewards of the Mg II $\lambda 2800$ emission (these objects are also called “overlapping trough” QSOs or OFeLoBALQs; see e.g. [Lucy et al. 2014](#); [Hall et al. 2002](#)). A detailed analysis of such complex systems is non-trivial and requires a dedicated approach (e.g. [Choi et al. 2020](#)) which is beyond the scope of this paper. Here we provide only a qualitative description of the most relevant features we detected on the QUIP FeLoBAL spectra, which are displayed in [Figure 6](#).

J0514–3854 ($z_{\text{em}} = 1.775$, $\alpha = -2.14$). A QSO with a strong Mg II emission, which corroborates the redshift estimation, mainly based on H α (which falls within a telluric band and may appear distorted for this reason; significant residuals of telluric removal are observed at $\lambda_{\text{rf}} \simeq 4950 \text{ \AA}$ and $\lambda_{\text{rf}} \simeq 6740 \text{ \AA}$). Broad Si IV, Al III, Fe II, and Mg II absorption lines are observed, confirming the identification as a FeLoBALQ. The absorption system has a complex velocity structure with at least three components; the strongest one has a redshift $z = 1.678$. No saturated trough is present. An absorption system at $\lambda_{\text{rf}} \simeq 1970 \text{ \AA}$ has no secure identification.

J1215–2129 ($z_{\text{em}} = 1.464$, $\alpha = -1.94$). Possibly the most peculiar of all QUIPs. The emission redshift is firmly determined by a strong H α line, despite the fact that H β is weak and H γ barely detected, and is compatible with an associated absorber at $z = 1.463$, observed in Mg II, Fe II, C IV (the identification of these species must be regarded as tentative). The main absorption line exhibits a wide and shallow profile, which probably emerges from an unresolved velocity structure. No line appears to be saturated.

J1318–0245 ($z_{\text{em}} = 1.404$, $\alpha = -2.06$). A BALQ with a strong associated absorption system at $z = 1.390$, observed in Mg II ad Fe II, at $\Delta v \simeq -1.8 \times 10^3 \text{ km/s}$ with respect to the emission redshift, securely determined from the Balmer series (H α , H β , and H γ). A second saturated system is likely identified as Mg II at $z = 1.344$, but lacks a clear Fe II counterpart. The region bluewards from the Fe II absorption is populated by several systems that could be identified only through accurate modeling, which is beyond the scope of this paper.

J1503–0451 ($z_{\text{em}} = 0.929$, $\alpha = -1.99$). At $z_{\text{em}} = 0.930$, this is the lowest-redshift QUIP in our list. The emission redshift is consistent with the possible identification of Pa $\gamma \lambda 1094$; a possible Mg II emission is almost completely suppressed by an associated absorber at $z = 0.923$, which is observed also in Fe II. This absorption system also includes a lower-redshift component ($z = 0.888\text{--}0.892$) and a not clearly resolved Fe II component at slightly higher redshift. Fe II resonance is also observed at shorter wavelengths; accurate modeling is required for a detailed identification of all the absorption features.

J2012–1802 ($z_{\text{em}} = 1.275$, $\alpha = -1.92$). Also this QSO show emission lines other than the Balmer series (O II $\lambda 3729$, Mg II); Mg II in particular appears to be partly obscured by an associated absorber at $z = 1.261$, observed also in Fe II, and Al III. In fact, at least two other absorption systems with the same transitions are observed at $z = 1.175$ and $z = 1.036$. These three systems together explain most of the strongest feature observed along the line of sight; as in the other cases, the level of unabsorbed continuum is hard to determine and blended absorption may actually be responsible for a consistent decrement in the observed flux bluewards of the Mg II emission.

J2018–4546 ($z_{\text{em}} = 1.352$, $\alpha = -1.85$). This QUIP is a quite clear example of OFeLoBALQ, with an almost completely saturated absorption trough bluewards of Mg II emission. Two associated Mg II/Fe II broad absorption lines are observed at the emission redshift and at $\Delta v \simeq -8.5 \times 10^3 \text{ km/s}$ with respect to the emission redshift ($z = 1.286$; this one possibly including Fe II $\lambda 2344$ alongside Fe II $\lambda 2382, 2600$). Partial coverage likely accounts for the fact

that the lines do not reach the zero level, despite exhibiting a clearly saturated profile. The amount of blended absorption prevents the secure identification of additional systems along the line of sight.

J2105–4104 ($z_{\text{em}} = 2.247$, $\alpha = -2.08$). This object shows features typical of both LoBALQs (Mg II, Fe II, Al III absorption) and HiBALQs (Si IV, C IV absorption). Low-ionization absorbers are observed at $z = 2.231, 2.153$; a narrower system (possibly a mini-BAL) is observed along the line of sight at $z = 1.568$ (at $\Delta v \approx -6.3 \times 10^4$ km/s). High-ionization absorbers, on the other hand, are observed at $z = 2.215, 2.085, 2.026, 1.926$. These identifications are not enough to explain all the absorption lines bluewards of the Mg II emission; most of these lines are narrow (FWHM $\sim 10^3$ km/s) and not too much affected by blending.

J2154–0514 ($z_{\text{em}} = 1.629$, $\alpha = -1.92$). For this QSO, the Balmer series is complemented by marginally detected Mg II and possibly Al III emission lines. An almost saturated system is observed at $z = 1.611$ ($\Delta v \approx -2.1 \times 10^3$ km/s) in Mg II, Fe II, and Al III; Fe II is particularly strong, corroborating the identification of this QUIP as a FeLoBALQ. The system may have an absorption “tail”, observed for Mg II at $\lambda_{\text{rf}} \approx 2630 \text{ \AA} - 2760 \text{ \AA}$ and for Fe II $\lambda 2600$ at $\lambda_{\text{rf}} \approx 2420 \text{ \AA} - 2540 \text{ \AA}$. A second weaker system at $z = 1.563$ is observed only in Mg II and Fe II $\lambda 2382$, and a third system at $z = 1.069$ in Mg II and Fe II $\lambda \lambda 2382, 2600$. Also in these cases, a dense pattern of absorbers below $\lambda_{\text{rf}} \approx 1800 \text{ \AA}$ is lacking a secure identification.

3.2 Other QSOs

Some QUIP targets do not show significant Fe II absorption in their spectra, and derive their peculiar character from individual features (most notably, broad metal absorption complex at high ionization) which are described in more detail below. We include in this group also the non-QUIP targets that were selected for NIR observations, to secure their identification.

J0008–5058 ($z_{\text{em}} = 2.041$, $\alpha = -1.89$). This QSOs shows an extended list of clearly detected emission lines at the emission redshift in addition to the Balmer series, including Mg II, C III, Al III, C IV, Si IV, Si III, N V, and Ly α . An associated absorber at $z = 2.0113$ ($\Delta v \approx -3.0 \times 10^3$ km/s) is observed in Mg II, Al III, C IV, Si IV, N V, and Ly α , identifying this object as a HiBALQ. A second component of this absorber at $z = 1.986$ ($\Delta v \approx -5.4 \times 10^3$ km/s) is possibly observed in C IV and Ly α . Other absorption lines bluewards of the Mg II emission remain unexplained.

J0010–3201 ($z_{\text{em}} = 2.379$, $\alpha = -2.05$). Another HiBALQ, exhibiting a particularly strong C IV/Si IV forest with at least two BAL features. Emission lines of Mg II, Al III, and C IV at the redshift of the Balmer series appear significantly masked by an absorber at slightly higher redshift ($z = 2.393$, $\Delta v \approx 1.2 \times 10^3$ km/s). Two possible BAL systems, almost saturated in C IV, Si IV, and Ly α , are observed at $z = 2.295$ and $z = 2.126$ (with absorption also in Mg II, Al III, and N V). Both systems display complex velocity patterns that we did not try to model, but give rise to comparable line profiles in C IV, Si IV, and Ly α .

J0140–2531 ($z_{\text{em}} = 2.947$). This QUIP has the second highest redshift in our sample, mainly anchored to the relative position of the Mg II, C IV, and N V emission lines; Ly α and Ly β are marginally detected at the emission redshift. The object does not appear to

be BALQ, showing only relatively weak absorptions in C IV and Si IV at $z = 2.848$ and $z = 2.746$ (the redder of the two absorbers, which is also the stronger, has also a clear H I counterpart). The Ly α forest along the line of sight to this object also appears relatively under-absorbed. A strong absorption at $\sim 1050 \text{ \AA}$ rest-frame may be associated to a S IV $\lambda 1063$ resonance closer to the emission redshift.

J0407–6245 ($z_{\text{em}} = 1.289$, $\alpha = -1.95$). A LoBALQ with almost no detectable Fe II absorption, this object displays Mg II and Al III emission lines complementing the Balmer series (which appears comparatively weaker than in other objects); the low-ionization metal emission is not entirely suppressed by an associated absorber slightly more redshifted than the QSO itself ($z = 1.310$, corresponding to $\Delta v \approx 2.7 \times 10^3$ km/s with respect to the emission redshift). A strong Mg II/Al III absorption system with a complex velocity structure is observed bluewards of the emission, with at least two components at $z = 1.227$ and $z = 1.193$ ($\Delta v \approx -8.2 \times 10^3$ km/s and -1.29×10^4 km/s respectively). Sparse absorption bluewards of the Mg II emission may be possibly due to Fe II, an hypothesis that could only be confirmed by an accurate modeling.

J2134–7243 ($z_{\text{em}} = 2.178$, $\alpha = -1.96$). A rather featureless, non-QUIP QSO, with no notable metal absorption complex at either high or low ionization. The redshift is determined mainly from the H α and Mg II emission lines; H β is very weak and H γ is undetected (it is expected to fall in a region of strong telluric absorption). Enhanced emission is observed at the emission redshift for Al III, C IV, and particularly Ly α ; the only unequivocal absorption feature is in fact identified as a Ly α , precisely at the QSO emission redshift.

J2157–3602 ($z_{\text{em}} = 4.665$, $\alpha = -1.42$). The relatively high redshift of this QSO is determined almost only on the basis of the Mg II emission line at $\lambda \approx 15 860 \text{ \AA}$, the Balmer series falling well outside the wavelength range covered by our observations; however, marginal detections of C II $\lambda 1908$, Al III, C IV, Si II, N V, and possibly also Si IV, Ly α , and O VI $\lambda 1037$ confirm the assessment. The QSO shows a strong associated metal system at $z = 4.608$ ($\Delta v \approx -3.0 \times 10^3$ km/s), observed in C IV, Si IV, N V and O VI; the corresponding Ly α and Ly β signatures are not too clear. A second Si IV/Si III absorption at $z = 4.438$ may have a correspondence in the Ly α (which is in general considerably opaque, as expected at this redshift); the whole region $\lambda \approx 7600 \text{ \AA} - 7900 \text{ \AA}$, bluewards of the Si IV $\lambda 1398$ emission is quite peculiar and possibly contaminated by uncorrected telluric absorption.

J2222–4146 ($z_{\text{em}} = 2.192$, $\alpha = -2.07$). A non-QUIP object quite similar to J2134–7243, with weak emission lines (H α and Mg II, constraining the emission redshift; H β , Si IV, Ly α) and no remarkable absorption feature outside the Ly α forest. Weak, extended absorption features bluewards of the Ly α emission lack a clear identification, as well as a strong absorption complex in the Ly α forest, at $\sim 1100 \text{ \AA}$ rest-frame, which may be associated to Fe III $\lambda 1123$. One could be led to categorize this QUIP as a BALQ, based on the latter complex, but the identification is uncertain and not corroborated by high- or low-ionization metal absorption.

J2255–5404 ($z_{\text{em}} = 2.255$, $\alpha = -2.19$). Another HiBALQ, with weak Al III and almost absent Mg II and Fe II absorption. Among the emission lines, H β is marginally detected and H γ is partly contaminated by a telluric band, but the determination of the emission redshift is secured, in addition to H α , by Mg II, C IV, N V, Ly α , and possibly Al III, Fe II $\lambda 1608$ (with a quite peculiar profile), Si IV, and

Si II. Two associated absorbers, redwards and bluewards of the QSO ($z = 2.283$ and $z = 2.234$, corresponding to $\Delta v \simeq 2.6 \times 10^3$ km/s and $\Delta v \simeq -1.9 \times 10^3$ km/s respectively) are observed in Al III, C IV, and Si IV; the low-redshift one (which is also the stronger) is observed also in Mg II, Fe II, Si II, N V, and Ly α , and appears to be slightly bluer for the low-ionization components ($z = 2.228$ instead of $z = 2.234$). A third strong metal absorber at $z = 2.160$ is also observed (Al III, C IV, Si IV, Si II, possibly Ly α).

J2319–7322 ($z_{\text{em}} = 2.612$, $\alpha = -1.88$). A HiBALQ with almost completely saturated C IV/Si IV forest. Emission lines are generally very weak (H β , Al III, C IV), with the possible exception of H α , Mg II, and Ly α (which nevertheless appear to be strongly contaminated by nearby absorption). A relatively narrow associated system at $z = 2.558$ ($\Delta v \simeq -4.5 \times 10^3$ km/s) is observed in Mg II, Al III, C IV, N V, and also Si IV and Ly α , with a slight shift in velocity. Hints of another associated absorber, slightly redshifted with respect to z_{em} ($z = 2.702$, $\Delta v \simeq 7.4 \times 10^3$ km/s) are possibly seen in Al III and Ly α . Most of the remaining absorption can be explained with (roughly) two low-ionization components (Mg II, Al III) at $z = 2.457$ and $z = 2.359$ and four high-ionization components (C IV, Si IV) at $z = 2.486, 2.413, 2.359, 2.291$, the latter being consistent also with an almost totally absorbed through in the Ly α forest, in the range $\lambda_{\text{rf}} \simeq 1170 \text{ \AA} - 1210 \text{ \AA}$.

J2355–5253 ($z_{\text{em}} = 2.363$, $\alpha = -1.72$). Another rather featureless non-QUIP QSO, similar to J2134–7243 and J2255–5404. A relatively weak Balmer series (H α , H β , possibly H γ) is complemented by Mg II, Ly α , and possibly extended C IV emission in constraining z_{em} . Notable absorption is observed only in the Ly α forest. A correspondence between narrow absorption lines is found for a system at $z = 2.360$, observed in N V, C IV, and possibly Si IV. No evidence for a BALQ classification is found.

4 DISCUSSION

4.1 Fraction of BALQs

The classification of targets in our sample based on their BAL features is graphically represented in Figure 4. We observe that:

- Both previously confirmed QSOs (flag A) are BALQs. Their inclusion among the QUIP targets was prompted by the peculiar absorption trough at the blue end of the spectra. We refrain from generalizing from this observation, though, due to the very low number of flag-A objects in our sample (2 out of 15 QUIPs). Despite their different emission redshift, these two QSOs (J2018–4546 and J2157–3602) display qualitatively similar spectra, with a significant drop in flux at $\lambda_{\text{obs}} \simeq 6500\text{--}7000 \text{ \AA}$, almost completely suppressing the emission continuum in the *u*, *g*, and *r* bands. In the case of J2018–4546, the drop is due to metal absorbers (Mg II and Fe II) at $z \simeq 1.3$, while in the case of J2157–3602 it is an effect of the Ly α forest at $z < 4.6$.

- A relatively large fraction of newly confirmed QSOs (previously flag B) are BALQs (12 out of 16 flag-B candidates, 92.3%), with a marginal prevalence of LoBALQs over HiBALQs (8 v. 4). These objects failed to be identified as QSOs in our previous analysis (Paper I, Paper II) because of their pattern of strong absorption features (arising from either low- or high-ionization metal absorbers), which significantly altered the expected distribution of flux in the *u*, *g*, and *r* bands. The peculiarity that motivated their inclusion in the

QUIP sample is now totally reconciled with the QSO nature of these sources, thanks to the information provided by the NIR spectra.

- All but one non-BAL QSOs are not included in the QUIP sample. This is consistent with the interpretation that a peculiar spectral appearance arises as result of significant absorption associated with the emitting source or located along the line of sight. The only QUIP not identified as a BALQ is J0140–2531, the second highest-redshift object in our sample, whose QUIP nature is probably due to the combination of an unevenly absorbed Ly α forest and an excess emission around and redwards of Mg II.

The fraction of BALQs among the general QSO population, F_{BAL} , is typically assessed at $\sim 10\text{--}15\%$ (e.g. Hewett & Foltz 2003, from pre-SDSS data; Reichard et al. 2003; Trump et al. 2006; Knigge et al. 2008; Gibson et al. 2009, from different SDSS releases), based on C IV absorption observed in the optical band, and is possibly increasing with redshift (Allen et al. 2011). Higher fractions have been advocated by some authors from observations in other bands: Dai et al. (2008) measured $F_{\text{BAL}} \simeq 25\text{--}40\%$ (depending on the classification criterion) on a sample 2MASS-selected QSOs, while Bruni et al. (2019) obtained $F_{\text{BAL}} \simeq 24\%$ from targets of the WISSH quasar project. The fraction of LoBALQs among BALQs, $F_{\text{LoBAL/BAL}}$, is similarly uncertain, being assessed at $\sim 15\%$ (e.g. Sprayberry & Foltz 1992; Reichard et al. 2003; Farrah et al. 2007) and possibly ranging between $\sim 5\text{--}30\%$ (Bruni et al. 2019). FeLoBALQs appear to be particularly rare, with estimates of $F_{\text{FeLoBAL/BAL}}$ as low as some percent (Trump et al. 2006; Dai et al. 2012).

The fraction of FeLoBALQs currently confirmed among QUBRICS QSOs is 8 out of 511 ($\sim 2\%$). We interpret this evidence as a consequence of the criteria adopted by the QUBRICS survey to select QSOs at $z > 2.5$ (Paper I). The selection procedure was trained to interpret a relative dearth of flux in the *g* band and in the bands bluewards as a signature of the Ly α forest in the relevant redshift range. A similar signature can nevertheless be produced by metal absorbers at lower redshift, provided they are strong enough to significantly impact the transmission in the band. QSOs at $z < 2.5$ with strong associated metal absorption can thus be mistaken as QSOs at $z > 2.5$, and at the same time be regarded as peculiar because their emission redshift cannot be properly assessed from optical spectra alone. The same occurrence was observed also in the SkyMapper survey, where a large fraction of low-redshift contaminants (16 out of 24) were identified as FeLoBALQs (Wolf et al. 2019). In particular:

- In the case of HiBALQs, C IV and Si IV absorption can mimic the appearance of the Ly α in the *g* band for $1.8 \lesssim z \lesssim 2.6$. All the HiBALQs in our sample are consistent with this range, with the exception of J2157–3602 (which shows a significantly absorbed Ly α forest in the *g* and *r* bands, and is regarded as a QUIP due to a peculiar absorption feature at $\lambda \simeq 7600\text{--}7900 \text{ \AA}$); if we neglect the outlier, the remaining targets have $z_{\text{H}} = 2.32 \pm 0.24$.

- In the case of LoBALQs, Mg II and Fe II complexes can similarly mimic the appearance of the Ly α in the *g* band for $0.6 \lesssim z \lesssim 1.8$. This explains both the redshift distribution of LoBALQs and FeLoBALQs in our sample ($z_{\text{L}} = 1.48 \pm 0.37$; $z_{\text{F}} = 1.50 \pm 0.39$) and the high fraction of detected FeLoBALQs: only LoBALQs with significantly strong Fe II absorption are likely to be mistaken for QSOs at higher redshift, due to the superficial similarity between the Ly α forest and the Fe II complexes.

The serendipitous discovery of 8 FeLoBALQs among the 18 QSOs discussed in this paper presents a noteworthy addition to the overall census of FeLoBALQs, not only in the Southern Hemisphere but in the whole sky. We remark that the relatively high fraction of

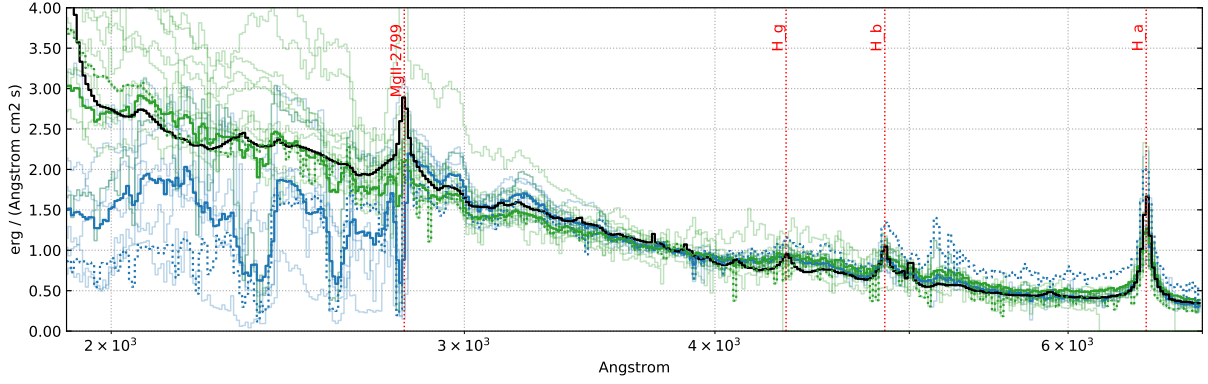


Figure 3. Composite rest-frame spectra of FeLoBALQs (blue) and non-FeLoBALQs (green) from our catalogue. De-reddened composites are shown with solid lines, while non-de-reddened composites are shown with dashed lines. The de-reddened spectra of the individual QSOs are shown in transparency; spectra are normalized at 3800 Å rest-frame to create the composites. The black solid line is the QSO template combined from Vanden Berk et al. 2001 and Glikman et al. 2006.

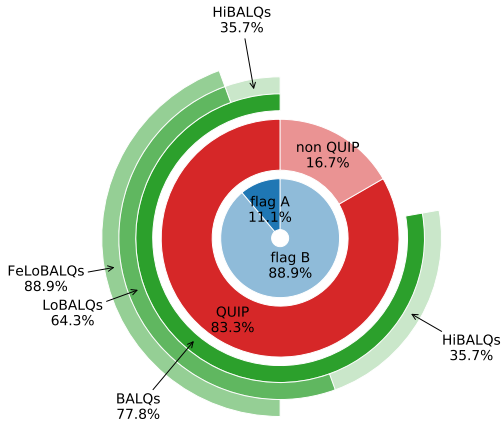


Figure 4. Classification of targets in our sample. Moving from the centre outwards, the rings display: 1. (blue) classification from Paper I; 2. (red) classification from current paper; 3. (green) distribution of BALQs among the previous groups; 4. (green) distribution of HiBALQs and LoBALQs among BALQs; 5. (green) distribution of FeLoBALQs among LoBALQs. Percentages in ring 4 refer to ring 3, while percentages in ring 5 refer to ring 4.

identified FeLoBALQs in our survey ($\sim 2\%$, see above) is computed over a population of QSOs at higher redshift ($z > 2.5$), which at magnitudes $i < 18$ have a lower surface density with respect to QSOs in the same redshift range of our FeLoBALQs ($0.6 \lesssim z \lesssim 1.8$). This fraction is therefore not directly comparable with the lower fraction from the literature (Trump et al. 2006; Dai et al. 2012), which is computed over matching redshift ranges for the FeLoBALQs and the general QSO population.

In other respects, the QSOs in our sample (both QUIPs and non-QUIPs) are not peculiar. The distributions of continuum slopes indexes (see subsection 2.3) give $\alpha_F = -1.98 \pm 0.09$, $\alpha_{nF} = -1.83 \pm 0.19$, with no dependence on redshift on either group (Figure 2). This value is in agreement with the literature (e.g. Cristiani et al. 2016). The small size of our sample, combined with the relatively high uncertainty associated with the flux calibration and continuum fitting procedure, prevents us from drawing stronger conclusions on this point.

Table 3. Black hole masses and Eddington ratios computed from line FWHMs and luminosities in Table 2, using formulae in subsection 4.2. The errors are propagated from FWHM and L measurements and do not reflect the intrinsic scatter of the distribution. Estimates from Equation 1 and 3 are in roman while estimates from Equation 2 and 4 are in italic.

QUBRICS ID	class	$\log M_{\text{BH}}/M_{\odot}$	$\log \lambda_{\text{Edd}}$
J0008-5058	Q,H	10.2 ± 0.1	-0.81 ± 0.13
J0010-3201	Q,H	10.3 ± 0.1	-0.87 ± 0.10
J0140-2531	Q		
J0407-6245	Q,L	9.6 ± 0.1	-0.38 ± 0.15
J0514-3854	Q,F	10.0 ± 0.1	-0.97 ± 0.1
J1215-2129	Q,F	10.3 ± 0.1	-1.11 ± 0.12
J1318-0245	Q,F	9.3 ± 0.2	-0.30 ± 0.15
J1503-0451	Q,F	10.1 ± 0.1	-1.00 ± 0.07
J2012-1802	Q,F	9.9 ± 0.1	-0.38 ± 0.10
J2018-4546	Q,F	10.3 ± 0.1	-0.71 ± 0.11
J2105-4104	Q,F	9.8 ± 0.1	0.05 ± 0.09
J2134-7243		9.75 ± 0.15	-0.79 ± 0.16
J2154-0514	Q,F	9.6 ± 0.1	-0.25 ± 0.11
J2157-3602	Q,H		
J2222-4146		10.3 ± 0.2	-1.10 ± 0.24
J2255-5404	Q,H	10.2 ± 0.1	-0.59 ± 0.1
J2319-7322	Q,H	9.9 ± 0.14	-0.78 ± 0.15
J2355-5253		8.9 ± 0.2	-0.13 ± 0.18

4.2 Reddening and Eddington ratios

Despite the low accuracy in the measurement of the intrinsic $E(B - V)$, FeLoBALQs in our sample are significantly more reddened than other QSOs, with $E(B - V)|_F = 0.15 \pm 0.08$, compared to $E(B - V)|_{nF} = 0.03 \pm 0.05$. This is consistent with higher levels of dust extinction (e.g. Sprayberry & Foltz 1992; Reichard et al. 2003; Gibson et al. 2009). As shown in Figure 3 Fe II absorption bluewards of ~ 2700 Å rest-frame is responsible for a decrease in the observed flux ranging from a factor of 2 to 3, most noticeable in correspondence of the absorbing features at ~ 2350 Å and ~ 2600 Å. Apart from these differences, the non-de-reddened composite of FeLoBALQs and non-FeLoBALQs do not look excessively different redwards of the Mg II emission (dashed lines in Figure 3). De-reddening accounts only for a marginal increase in continuum steepness at $\lambda > 3000$ Å. The overall shape of the emission lines alone provide no indication of a difference between the two groups.

The parameters of the H α and H β lines extracted by QSFIT as discussed in subsection 2.3 can be used to estimate the mass M_{BH}

of the black holes powering the QSOs that we observed, albeit with limited accuracy. We adopted two different M_{BH} estimates:

- M_{BH}^{5100} , using the $\text{H}\beta$ broad component FWHM and the optical continuum luminosity at 5100 Å (Vestergaard & Peterson 2006, Equation 5):

$$M_{\text{BH}}^{5100} = 10^{5.91} \left[\frac{\text{FWHM}_{\text{H}\beta}}{1000 \text{ km s}^{-1}} \right]^2 \left[\frac{\lambda L_{5100}}{10^{42} \text{ erg s}^{-1}} \right]^{0.50} M_{\odot}; \quad (1)$$

- $M_{\text{BH}}^{\text{H}\alpha}$, using the $\text{H}\alpha$ broad component FWHM and luminosity (Schulze et al. 2017, Equation 2):

$$M_{\text{BH}}^{\text{H}\alpha} = 10^{6.711} \left[\frac{\text{FWHM}_{\text{H}\alpha}}{1000 \text{ km s}^{-1}} \right]^{2.12} \left[\frac{\lambda L_{\text{H}\alpha}}{10^{42} \text{ erg s}^{-1}} \right]^{0.48} M_{\odot}; \quad (2)$$

We also computed the Eddington ratios $\lambda_{\text{Edd}} = L_{\text{bol}}/L_{\text{Edd}}$ using two different bolometric corrections:

- Shen et al. (2011) for L_{5100} :

$$\lambda_{\text{Edd},5100} \approx 9.26 L_{5100} / 1.25 \times 10^{38} M_{\text{BH}}^{5100}; \quad (3)$$

- Stern & Laor (2012) for $L_{\text{H}\alpha}$:

$$\lambda_{\text{Edd},\text{H}\alpha} = 130 L_{\text{H}\alpha} / 1.25 \times 10^{38} M_{\text{BH}}^{\text{H}\alpha}. \quad (4)$$

The virial mass estimators in the equations above are calibrated using relatively low- z sources, whose $\text{H}\alpha$ and $\text{H}\beta$ emission lines are still observable in the optical wavebands. Here we are extrapolating their usage to $z \gtrsim 2$, and since the luminosities increase with redshift we expect to find larger values for the black hole mass with respect to the population of QSOs at $z < 1$ (see discussion in §5.1 of Shemmer et al. 2004).

The estimated values of M_{BH} and λ_{Edd} for the QSOs in our sample are listed in Table 3. Only targets with a reliable line model (16 out of 18) were used to estimate the black hole mass. M_{BH}^{5100} (and consequently $\lambda_{\text{Edd},5100}$) was computed only for targets that allowed a proper modeling of the $\text{H}\beta$ line. In some cases (J0010–3201, J2222–4146, and J2319–7322), QSFIT provided only an upper limit for $\text{FWHM}_{\text{H}\beta}$; in other cases (J0008–5058, J0514–3854, J1215–2129, J2134–7243, J2255–5404, and J2355–5253), the $\text{H}\beta$ line appeared to be contaminated by telluric absorption or not prominent enough. For all these targets, $M_{\text{BH}}^{\text{H}\alpha}$ and $\lambda_{\text{Edd},\alpha}$ were used instead. We remark that our best fit model parameters should be considered rough estimates, and are provided as best effort values. Their limited reliability sums up with the significant uncertainties associated with single epoch virial mass estimates (~ 0.5 dex), providing no significant evidence for a tension between our mass values and the values from the literature (Figure 5).

Despite the limitations discussed in subsection 2.3, the continuum and emission line models obtained by QSFIT are reliable enough to map the distribution of λ_{Edd} across our sample (Figure 5). A comparison with the distribution of 230 luminous QSOs at redshift $1.5 < z < 4.0$ (Coatman et al. 2017, green crosses) and with the 18 WISE/SDSS selected hyper-luminous (WISSH) QSOs at $z \approx 2-4$ (Vietri et al. 2018, grey stars) shows an overall agreement. No statistically significant difference between FeLoBALQs and non-FeLoBALQs (filled and empty circles, respectively) is observed: we measured $\log \lambda_{\text{Edd},\text{F}} = -0.58 \pm 0.41$ for the former and $\log \lambda_{\text{Edd},\text{nF}} = -0.68 \pm 0.32$ for the latter; these values are consistent with those obtained by Schulze et al. (2017) and corroborate their conclusion that (Fe)LoBALQs do not appear to accrete at a higher rate compared to the general QSO population. Overall, no evidence to support an evolutionary scenario for (Fe)LoBALQs is observed.

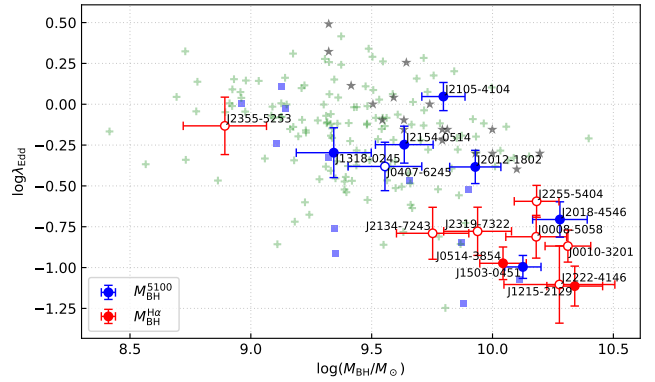


Figure 5. Eddington ratios estimated from QSFIT models of the targets in our sample. Blue dots are computed from Equation 1 and 3 while red dots from Equation 2 and 4. FeLoBALQs are denoted with filled circles, while other targets are denoted with empty circles. Light-blue squares are from Schulze et al. (2017); green crosses from Coatman et al. (2017); grey stars from Vietri et al. (2018).

5 CONCLUSIONS

We have presented the combined optical-to-NIR spectra of 18 QSOs from the QUBRICS survey (Calderone et al. 2019; Boutsia et al. 2020), which were previously unconfirmed or lacking a secure redshift estimation. Redshift values ranging from 0.928 to 4.665 have been determined for all objects with a fiducial uncertainty of 0.001, based on the identification of the Balmer series and/or Mg II emission lines made accessible by the NIR spectroscopy. Emission lines as well as several dozens of absorption systems, either associated with the emitting sources or intervening along the line of sight, have been detected using ASTROCOOK (Cupani et al. 2020b). The continuum emission has been modeled with QSFIT (Calderone et al. 2017), resulting in best-fit power-law slopes ranging from -2.19 to -1.42 .

In most cases (83.3% of the observed targets), the acquisition of NIR spectra was prompted by peculiarities in the already available optical spectra (hence the designation of “QUBRICS Irregular and Peculiar” targets, or QUIPs). An unexpectedly high fraction of targets have been identified as broad-absorption line quasars or BALQs (77.7% of the observed targets), and in particular BALQs with significant low-ionization Fe II absorption or FeLoBALQs (44.4% of the observed targets), with a great degree of superposition between the original QUIP assessment and the successive BALQ confirmation (93.3% BALQs among QUIPs). Such large detection rates arise as a serendipitous consequence of the selection criteria adopted by the QUBRICS survey: the procedure is optimized to identify QSOs at $z > 2.5$ through their $\text{Ly } \alpha$ forest, and is therefore triggered by significant metal absorption in the g band, leading to the identification of several BALQs (and especially FeLoBALQs) at $0.6 \lesssim z \lesssim 1.8$. This is a convenient result for all science cases relying on the statistical and individual analysis of such rare objects.

QUBRICS FeLoBALQs appear significantly more reddened than other QSOs (with an average colour excess of 0.015), confirming what observed by other studies (Sprayberry & Foltz 1992; Reichard et al. 2003; Gibson et al. 2009). However, the interpretation of the (Fe)LoBALQ phenomenon as an early stage in the QSO evolution is not supported by any evidence of increased accretion rate, as the mean Eddington ratio of FeLoBALQs is observed to be low (typically between 1 and 8 percent). The black hole masses measured across our whole sample (including both BALQs and non-BALQs) are con-

sistent with those measured for luminous QSOs by other authors (Coatman et al. 2017; Vietri et al. 2018), indicating no difference in the mass distribution of BALQs (and in particular FeLoBALQs). A better understanding of the individual characteristics of the FeLoBALQs in our sample would require further observations at higher resolution, e.g. with VLT X-shooter.

ACKNOWLEDGEMENTS

AG and FF acknowledge support from PRIN MIUR project ‘Black Hole winds and the Baryon Life Cycle of Galaxies: the stone-guest at the galaxy evolution supper’, contract 2017-PH3WAT.

GCU would like to thank Manuela Bischetti and Andrea Travascio for insightful discussion.

This work is based on data products from observations made with (1) ESO Telescopes at La Silla Paranal Observatory, Chile (ESO programmes ID 103.A-0746(A), 0103.A-0746(B), and 0104.A-0754(A)), (2) the 6.5 meter Magellan Telescopes located at Las Campanas Observatory, Chile, and (3) the Italian Telescopio Nazionale Galileo (TNG) operated on the island of La Palma by the Fundación Galileo Galilei of the INAF (Istituto Nazionale di Astrofisica) at the Spanish Observatorio del Roque de los Muchachos of the Instituto de Astrofísica de Canarias.

This work has made use of data from the European Space Agency (ESA) mission *Gaia* (<https://www.cosmos.esa.int/gaia>), processed by the *Gaia* Data Processing and Analysis Consortium (DPAC, <https://www.cosmos.esa.int/web/gaia/dpac/consortium>). Funding for the DPAC has been provided by national institutions, in particular the institutions participating in the *Gaia* Multilateral Agreement.

DATA AVAILABILITY

The spectra and the software tools described in this paper are made publicly available to ensure that the analysis is fully reproducible, and to foster a full exploitation of the collected data. The package has DOI [10.20371/INAF/DS/2021_000003](https://doi.org/10.20371/INAF/DS/2021_000003) and is available at <https://www.ict.inaf.it/index.php/31-doi/137-ds-2021-03>. It contains:

- Input spectra, i.e. reduced optical spectra;
- `ASTROCOOK` and `QSFIT` scripts, with instructions to run them;
- Output spectra and figures for reference.

REFERENCES

Allen J. T., Hewett P. C., Maddox N., Richards G. T., Belokurov V., 2011, *MNRAS*, **410**, 860

Boutsia K., et al., 2020, arXiv e-prints, p. arXiv:2008.03865

Boutsia K., et al., 2021, *ApJ*, **912**, 111

Bruni G., et al., 2019, *A&A*, **630**, A111

Calderone G., Nicastro L., Ghisellini G., Dotti M., Sbarbato T., Shankar F., Colpi M., 2017, *MNRAS*, **472**, 4051

Calderone G., et al., 2019, *ApJ*, **887**, 268

Choi H., Leighly K. M., Terndrup D. M., Gallagher S. C., Richards G. T., 2020, *ApJ*, **891**, 53

Coatman L., Hewett P. C., Banerji M., Richards G. T., Hennawi J. F., Prochaska J. X., 2017, *MNRAS*, **465**, 2120

Cristiani S., Serrano L. M., Fontanot F., Vanzella E., Monaco P., 2016, *MNRAS*, **462**, 2478

Cupani G., Calderone G., Cristiani S., Di Marcantonio P., D’Odorico V., Taffoni G., 2018, *Proc. SPIE*, **10707**, 1070723

Cupani G., Calderone G., Cristiani S., D’Odorico V., Taffoni G., 2020a, *Astronomical Society of the Pacific Conference Series*, **522**, 187

Cupani G., D’Odorico V., Cristiani S., Russo S. A., Calderone G., Taffoni G., 2020b, *SPIE Conference Series*, **11452**, 372

Dai X., Shankar F., Sivakoff G. R., 2008, *ApJ*, **672**, 108

Dai X., Shankar F., Sivakoff G. R., 2012, *ApJ*, **757**, 180

Di Matteo T., Springel V., Hernquist L., 2005, *Nature*, **433**, 604

Fabian A. C., 2012, *ARA&A*, **50**, 455

Farrah D., Lacy M., Priddey R., Borys C., Afonso J., 2007, *ApJ*, **662**, L59

Farrah D., et al., 2012, *ApJ*, **745**, 178

Faucher-Giguère C.-A., Quataert E., Murray N., 2012, *MNRAS*, **420**, 1347

Foltz C., Wilkes B., Weymann R., Turnshek D., 1983, *PASP*, **95**, 341

Gagné J., Lambrides E., Faherty J. K., Simcoe R., 2015, FireHose_v2: Firehose v2.0, [doi:10.5281/zenodo.18775](https://doi.org/10.5281/zenodo.18775), <https://doi.org/10.5281/zenodo.18775>

Gibson R. R., et al., 2009, *ApJ*, **692**, 758

Glikman E., Helfand D. J., White R. L., 2006, *ApJ*, **640**, 579

Guarneri F., Calderone G., Cristiani S., Fontanot F., Boutsia K., Cupani G., Grazian A., D’Odorico V., 2021, *MNRAS*, **506**, 2471

Hall P. B., et al., 2002, *ApJS*, **141**, 267

Hazard C., McMahon R. G., Morton D. C., 1987, *MNRAS*, **229**, 371

Hewett P. C., Foltz C. B., 2003, *AJ*, **125**, 1784

Kelson D. D., 2003, *PASP*, **115**, 688

Kelson D. D., Illingworth G. D., van Dokkum P. G., Franx M., 2000, *ApJ*, **531**, 159

Knigge C., Scaringi S., Goad M. R., Cottis C. E., 2008, *MNRAS*, **386**, 1426

Korista K. T., Voit G. M., Morris S. L., Weymann R. J., 1993, *ApJS*, **88**, 357

Kormendy J., Ho L. C., 2013, *ARA&A*, **51**, 511

Lazarova M. S., Canalizo G., Lacy M., Sajina A., 2012, *ApJ*, **755**, 29

Lu K.-X., Zhao Y., Bai J.-M., Fan X.-L., 2019, *MNRAS*, **483**, 1722

Lucy A. B., Leighly K. M., Terndrup D. M., Dietrich M., Gallagher S. C., 2014, *ApJ*, **783**, 58

O’Donnell J. E., 1994, *ApJ*, **422**, 158

Peterson B. M., Wanders I., Horne K., Collier S., Alexander T., Kaspi S., Maoz D., 1998, *PASP*, **110**, 660

Reichard T. A., et al., 2003, *AJ*, **126**, 2594

Schulze A., et al., 2017, *The Astrophysical Journal*, **848**, 104

Shemmer O., Netzer H., Maiolino R., Oliva E., Croom S., Corbett E., di Fabrizio L., 2004, *ApJ*, **614**, 547

Shen Y., et al., 2011, *ApJS*, **194**, 45

Silk J., Rees M. J., 1998, *A&A*, **331**, L1

Sprayberry D., Foltz C. B., 1992, *ApJ*, **390**, 39

Stern J., Laor A., 2012, *MNRAS*, **423**, 600

Tody D., 1993, in Hanisch R. J., Brissenden R. J. V., Barnes J., eds, *Astronomical Society of the Pacific Conference Series Vol. 52, Astronomical Data Analysis Software and Systems II*. p. 173

Trump J. R., et al., 2006, *ApJS*, **165**, 1

Urrutia T., Lacy M., Spoon H., Glikman E., Petric A., Schulz B., 2012, *ApJ*, **757**, 125

Vanden Berk D. E., et al., 2001, *AJ*, **122**, 549

Vestergaard M., Peterson B. M., 2006, *ApJ*, **641**, 689

Vietri G., et al., 2018, *A&A*, **617**, A81

Violino G., et al., 2016, *MNRAS*, **457**, 1371

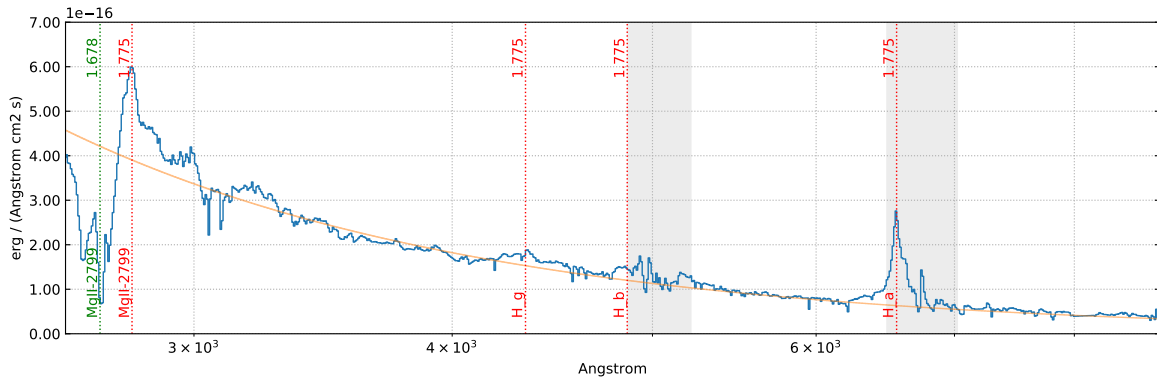
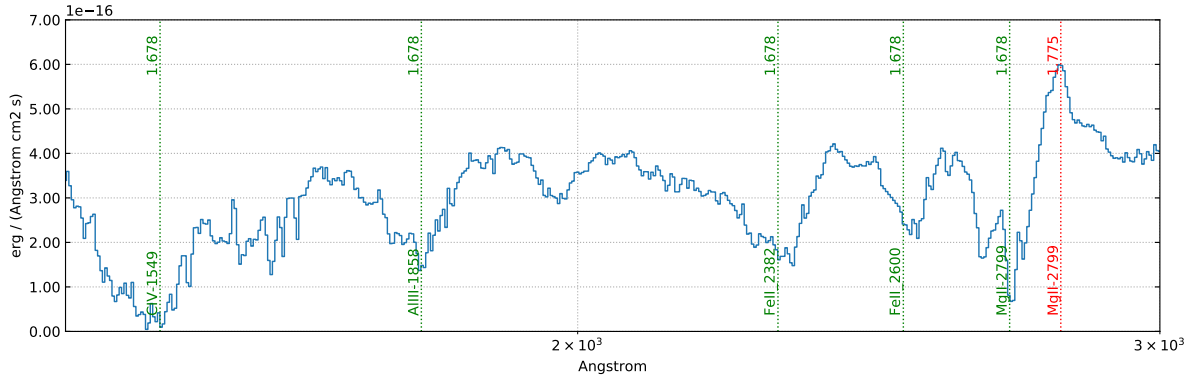
Weymann R. J., Morris S. L., Foltz C. B., Hewett P. C., 1991, *ApJ*, **373**, 23

Wolf C., et al., 2018, *Publ. Astron. Soc. Australia*, **35**, e010

Wolf C., et al., 2019, *Monthly Notices of the Royal Astronomical Society*, **491**, 1970

This paper has been typeset from a $\text{\TeX}/\text{\LaTeX}$ file prepared by the author.

J0514–3854 ($z_{em} = 1.775$, $\alpha = -2.15$)



J1215–2129 ($z_{em} = 1.464$, $\alpha = -1.98$)

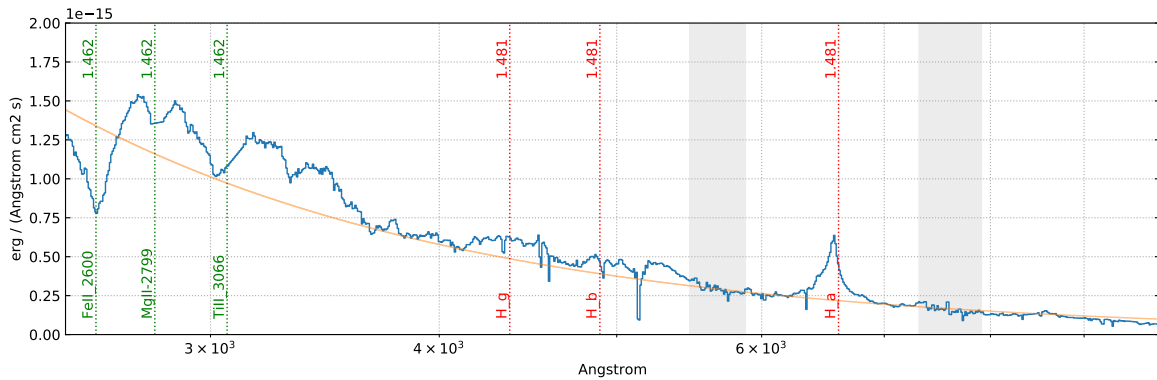
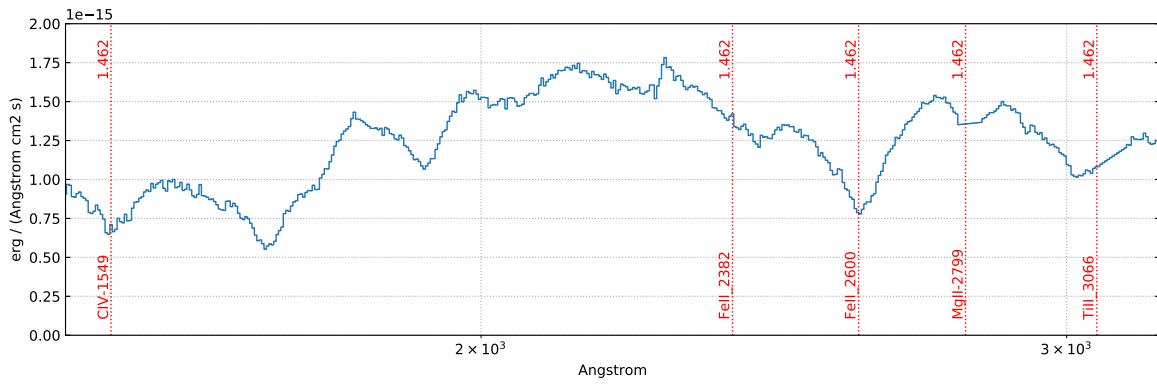
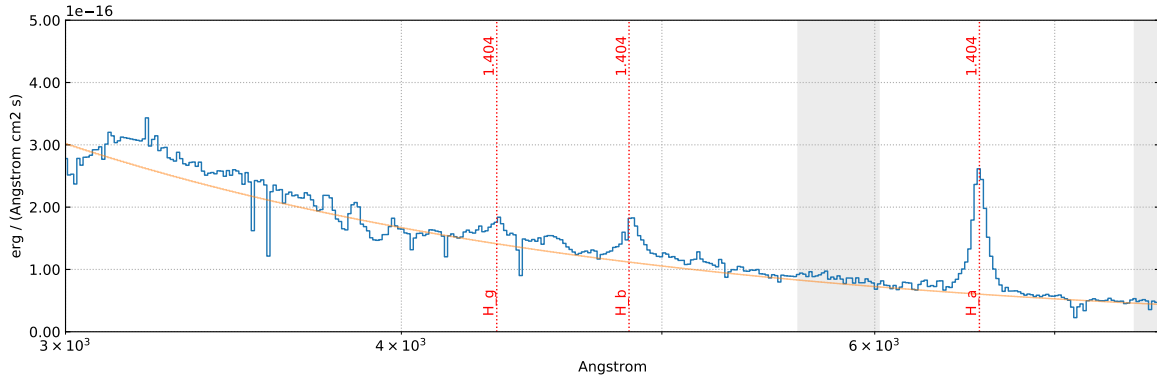
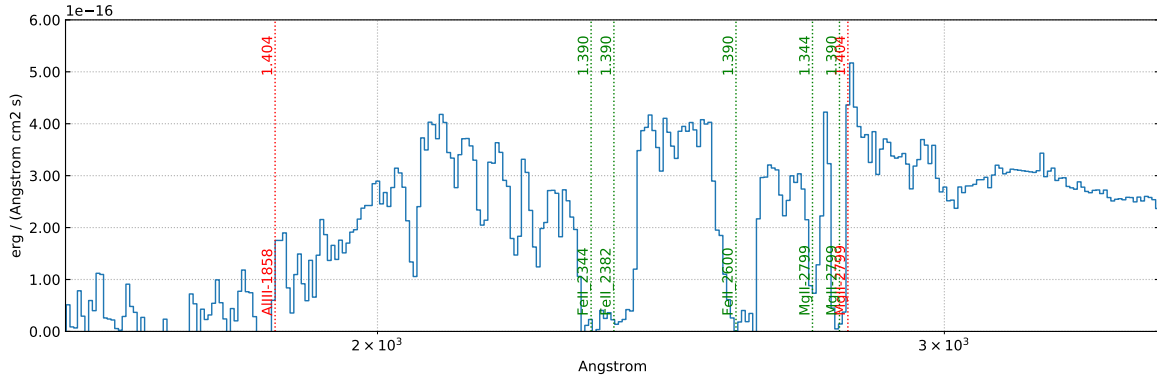


Figure 6. Spectra of FeLoBALQs from our sample. Wavelengths are rest-frame. Notable emission and absorption features are highlighted by dotted bars (red and green, respectively). Regions affected by strong telluric absorption are shaded. Each spectrum is split into two chunks for better visualization; in the red chunk, the best-fitting power-law continuum (orange line, see subsection 2.3) is superimposed to the extracted flux density (blue line). Some absorption lines may be omitted in the red chunk for better clarity.

J1318-0245 ($z_{em} = 1.404$, $\alpha = -2.06$)



J1503-0451 ($z_{em} = 0.929$, $\alpha = -1.96$)

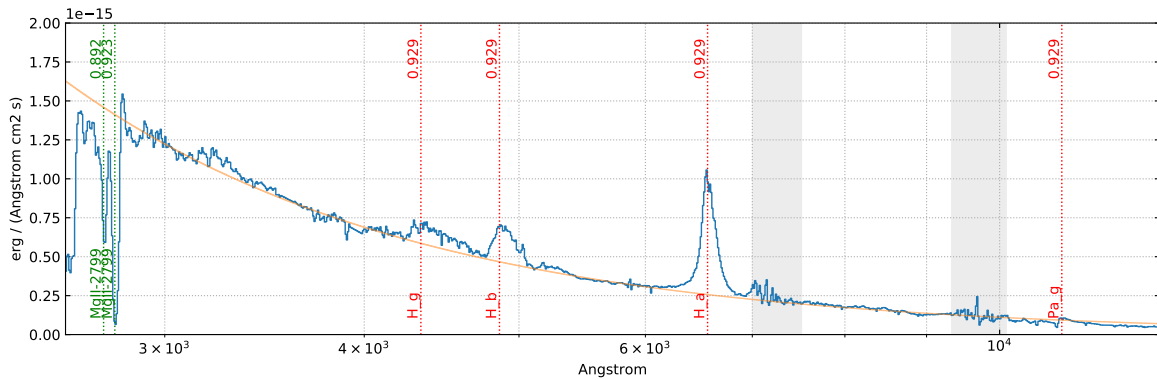
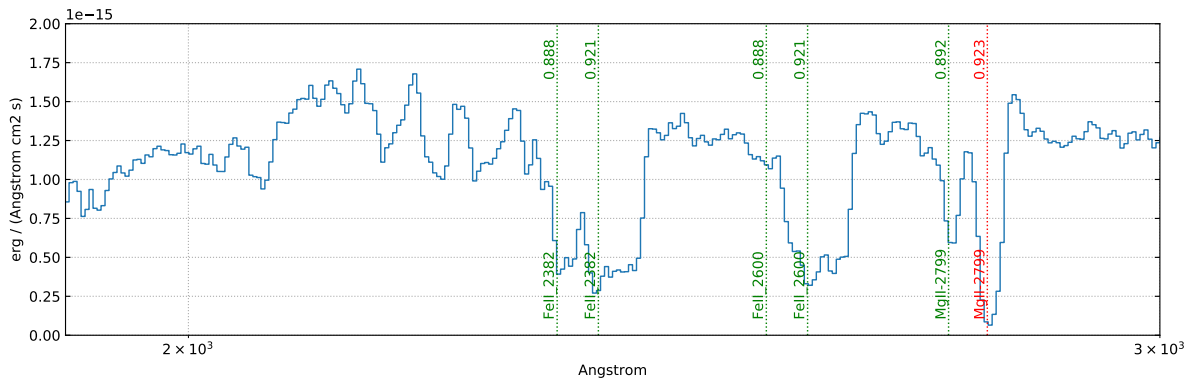
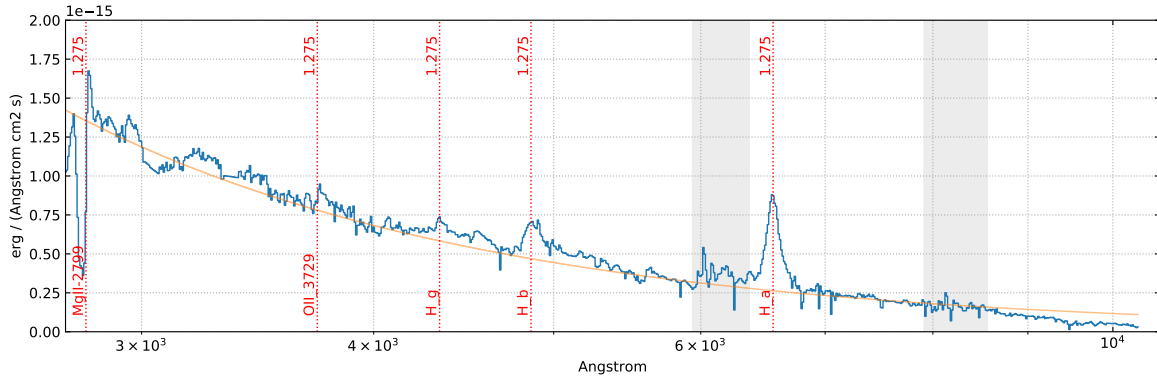


Figure 6 – continued

J1202–1802 ($z_{em} = 1.275, \alpha = -1.91$)



J1208–4546 ($z_{em} = 1.352, \alpha = -1.85$)

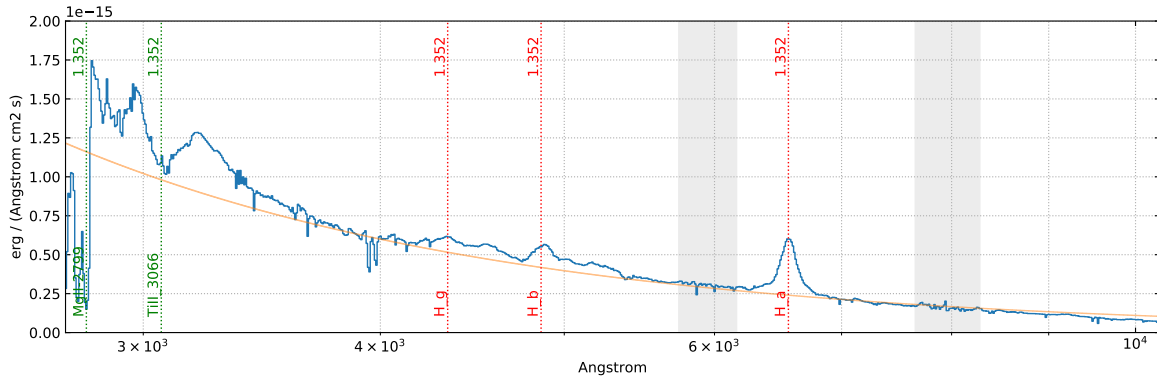
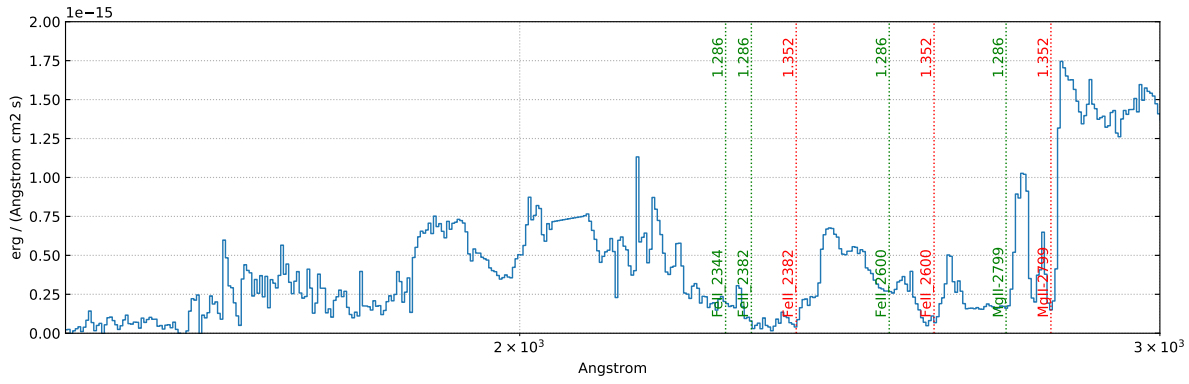


Figure 6 – continued

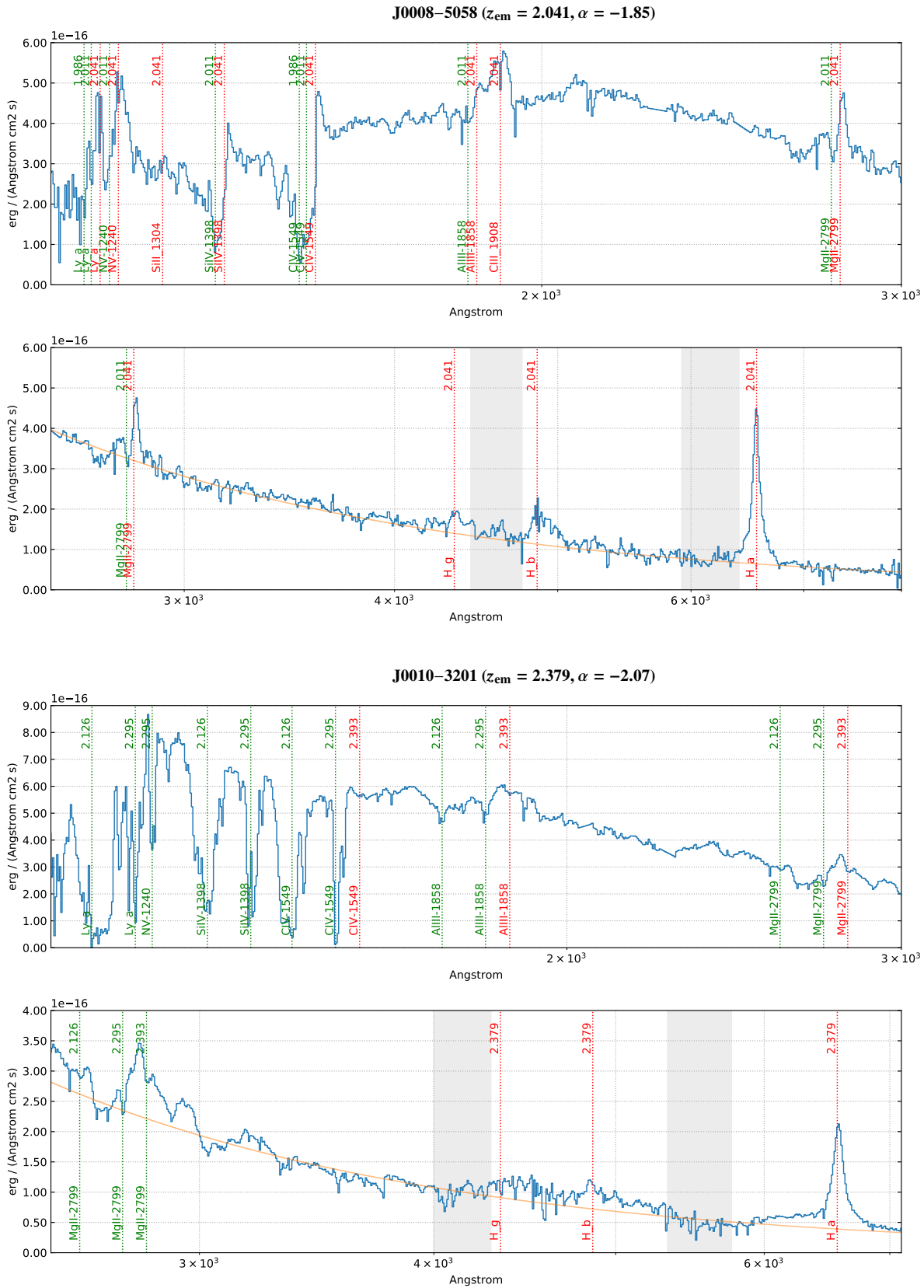
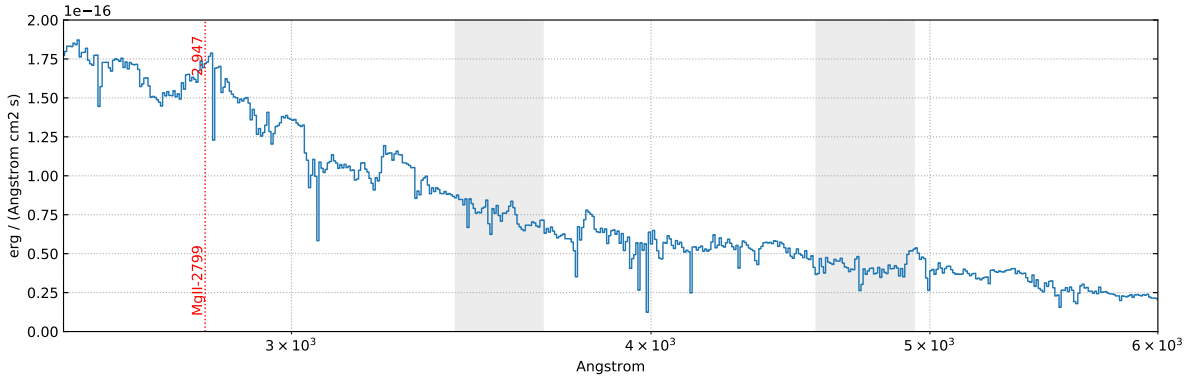
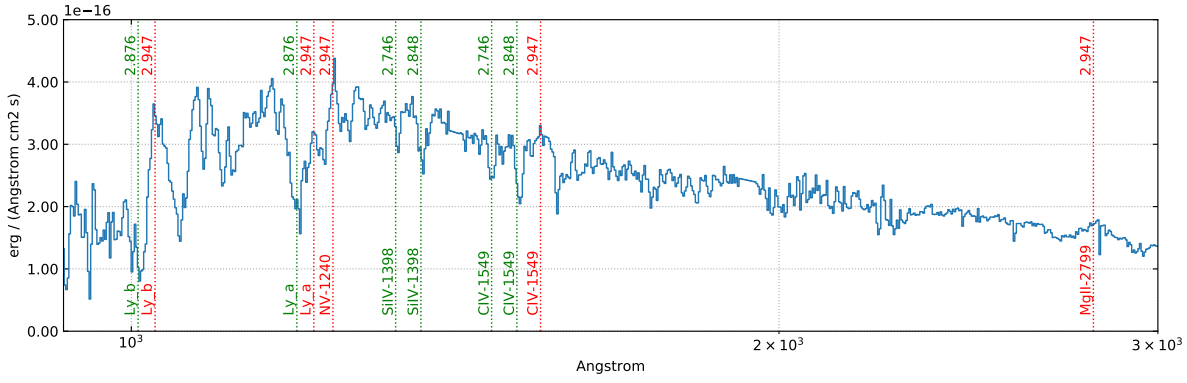


Figure 7. Spectra of other QUIP and non-QUIP QSOs from our sample. The legend is the same as Figure 6.

J0140–2531 ($z_{em} = 2.947$)



J0407–6245 ($z_{em} = 1.289$, $\alpha = -1.96$)

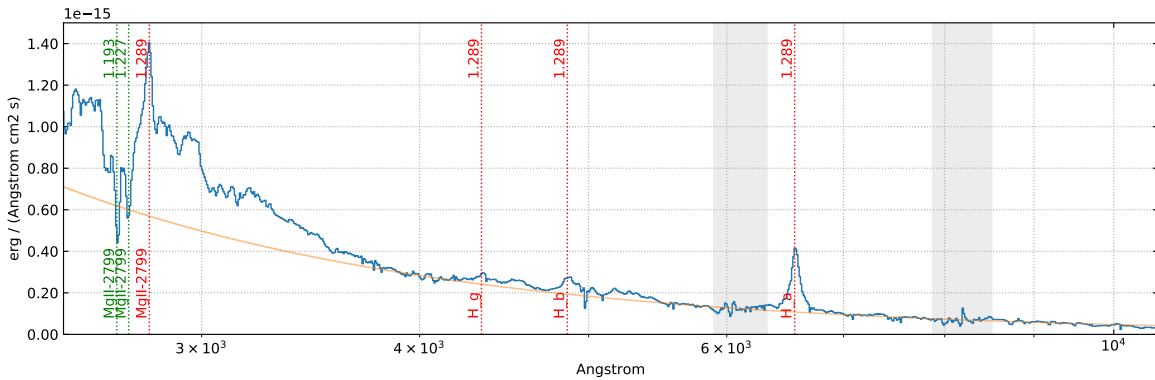
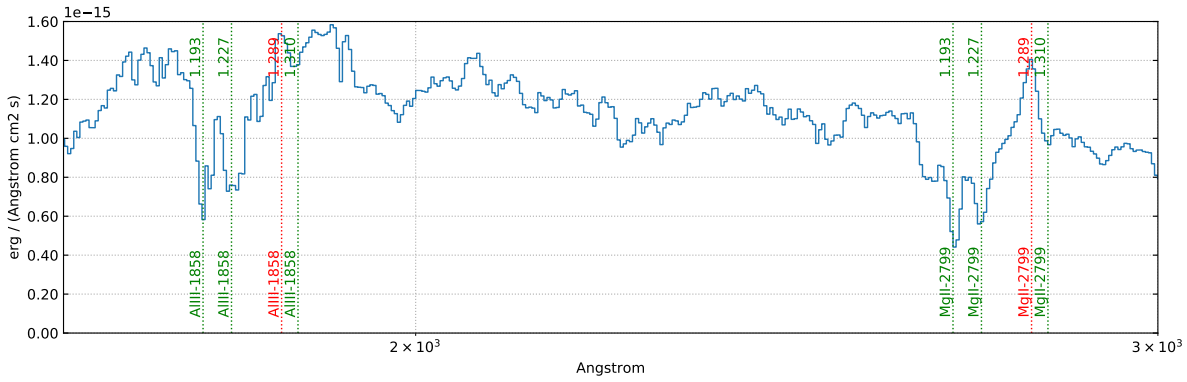
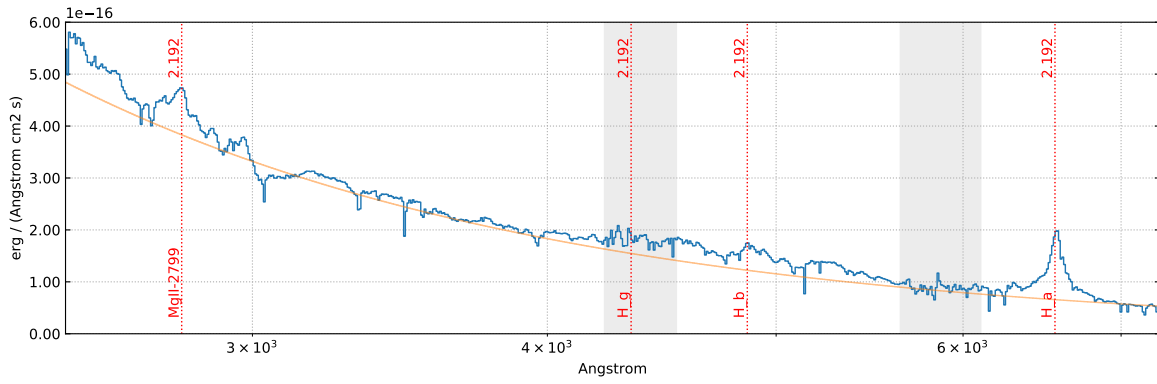
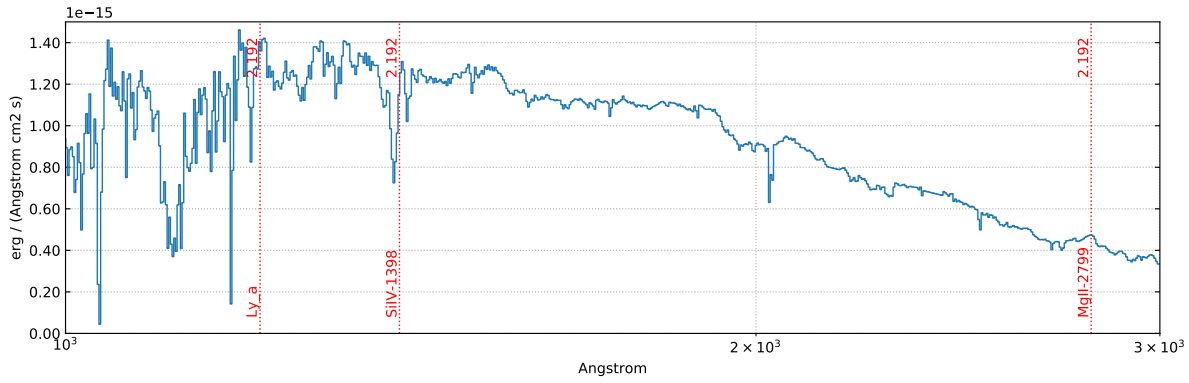


Figure 7 – continued

J2222–4146 ($z_{em} = 2.192$, $\alpha = -2.06$)



J2255–5404 ($z_{em} = 2.255$, $\alpha = -2.19$)

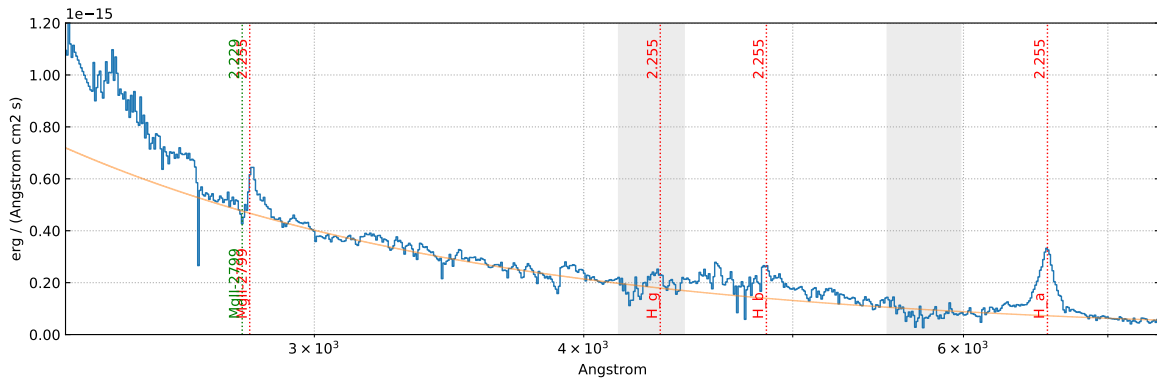
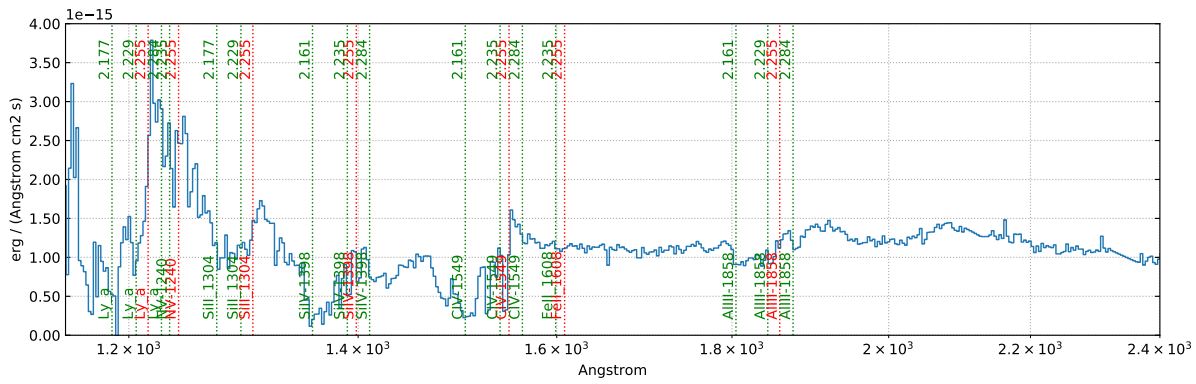
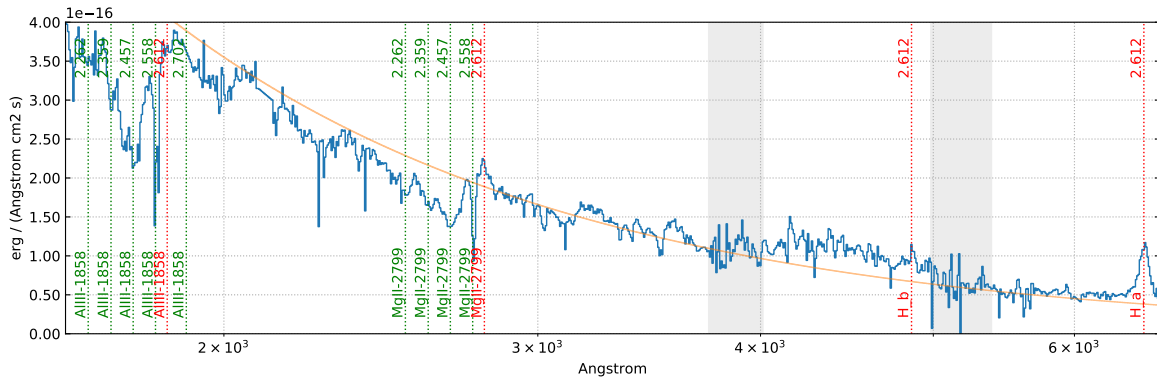
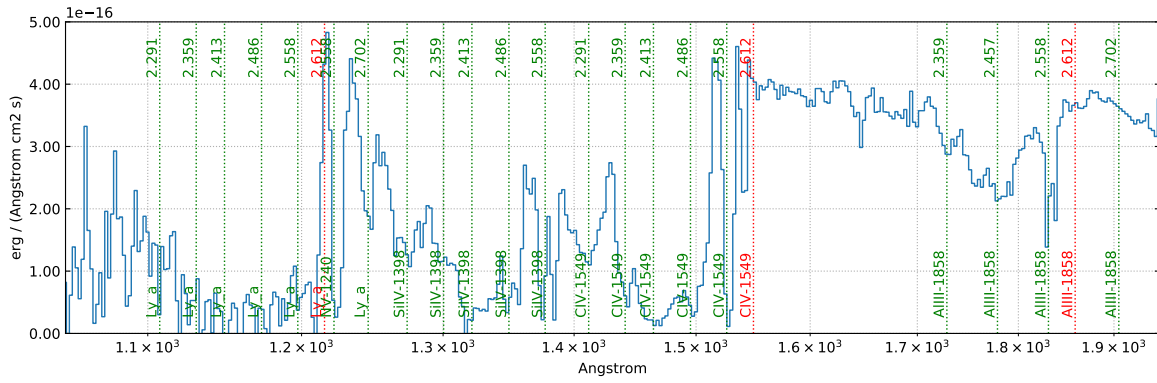


Figure 7 – continued

J2319–7322 ($z_{em} = 2.612, \alpha = -1.88$)



J2355–5253 ($z_{em} = 2.363, \alpha = -1.73$)

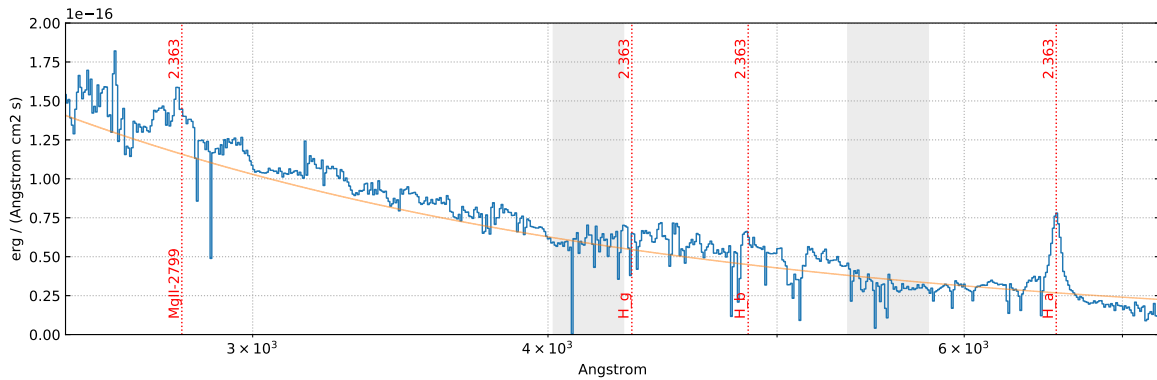
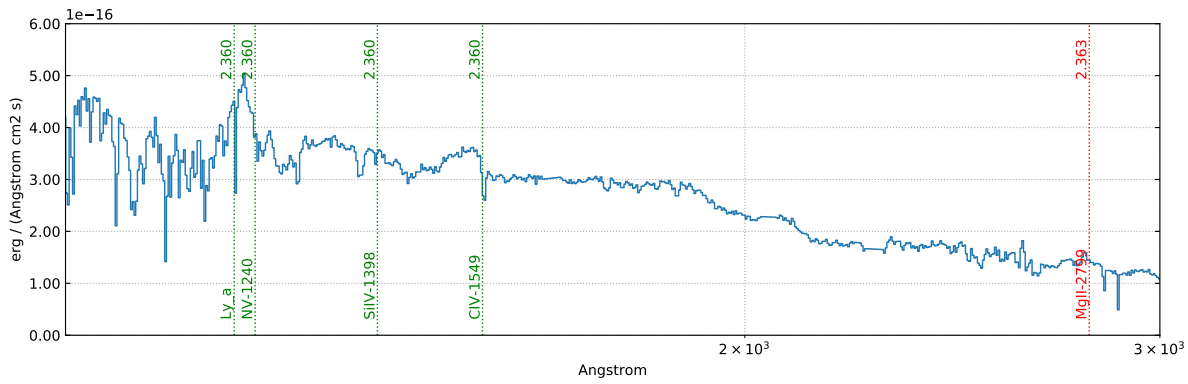


Figure 7 – continued